UNIVERSITY OF BIRMINGHAM

MSc by Research in Physics and Astronomy

Towards the study of topological defects in ^{87}Rb Bose-Einstein condensate

Author:
Jaime Sánchez Claros

Ultracold Atoms Group
School of Physics and Astronomy
College of Engineering and Physical Sciences
University of Birmingham
November 2019

To all those who have been always supporting me

Abstract

This master thesis describes my work as a Ph.D. student in the laboratory of the Quantum Gases group during one and a half year. The experiment creates spinor Bose Einstein condensates of $\sim 10^5$ atoms with a repetition rate of 12 seconds, using all-optical methods. I report a full description of the elements and techniques involved. My main contribution has been the building of a phase-imprinting apparatus in order to study different topological defects in the condensate. Currently, the apparatus is still in the testing phase, therefore I had the opportunity to reproduce only some initial results on the creation of solitons.

Contents

List of Figures

List of Tables

Chapter 1

Introduction

This master thesis is the result of my work of almost one year and a half as a PhD student in the Quantum Gases group of the University of Birmingham, under the supervision of Dr. Giovanni Barontini. I took part in an experiment focused on generating a 3-dimensional ^{87}Rb Bose-Einstein condensate (BEC) by all-optical methods. This means that Rubidium atoms, below a certain critical temperature, macroscopically occupy the lowest energy state, showing a coherent and collective behaviour. This behaviour allows us to describe the system by a macroscopic wave function. Quite curiously, it took around 70 years from the theoretical prediction by Satyendra Nath Bose and Albert Einstein until its experimental observation in dilute Alkali metal gases by Davis *et al.* [4] in 1995. Nowadays many physicists, both experimentalists and theorists, still investigate the physics that surrounds this state of matter and its diverse applications.

The goal of the project consists in studying different kind of non-linear dynamics by manipulating the Bose-Einstein condensate. These non-linear effects depend on the type of interaction between the bosons, and are due to topological defects. The most simple topological defects are vortices [5] and solitons [6]. A really interesting topological case is the Berezinskii-Kosterlitz-Thouless (BKT) phase transition [7, 8] that occurs in 2-dimensional systems. The BKT theory associates this transition with the emergence of pairs of vortices with opposite circulation [9]. Moreover, the manipulations of the condensate also allow to perform simulations of high-energy Physics, e.g., the observation of the Andreev-Bashkin effect which determines the behaviour of neutron stars [10]. This master thesis is structured as follows.

In chapter 2, I explain how the experimental set-up works, and I discuss the correspondent theoretical basis of the techniques employed in order to achieve Bose-Einstein condensation. These techniques include laser cooling, magneto-optical traps, and evaporative cooling.

The third chapter is focused on my main contribution in this project: the installation of a set-up to implement the phase-imprinting technique. This technique consists in imposing light patterns which modify the phase of the wave function, giving rise to topological defects. The required elements are: a spatial light modulator which creates the patterns,

a demagnifying optical system which allows to focus the pattern onto the condensate, and the generation of a time-averaged potential. The latter is useful for the implementation of the phase-imprinting technique, as I will explain later.

In chapter four, I show the first results obtained using the phase-imprinting method to generate solitons. In the literature, there are many available works, both theoretical and experimental, which discuss the dynamics of solitons. This makes the generation of solitons a test to check the proper functioning of the technique.

Chapter 2

The experimental sequence

In this chapter, I will show how the experimental platform has been realized and how it works in order to get a pure ^{87}Rb Bose-Einstein condensate by all-optical methods. First, I will present a brief theoretical introduction to laser cooling and trapping, explaining the basics of molasses, magneto-optical traps, and dipole traps. This will help to understand the working principle of the experiment. After that, I will explain step by step the technical requirements of the experiment, including the schematics of the set-up.

2.1 Laser cooling and trapping

As mentioned before, in this section I will introduce the techniques required for cooling down and trapping atoms. First of all, it is worth providing a brief introduction to the hyperfine structure of ^{87}Rb, in order to understand the requirements for the laser sources that the experiment needs.

2.1.1 Hyperfine structure of ^{87}Rb

Alkali atoms have a hydrogen-like structure with only one valence electron. This property makes laser cooling a relatively simple process [11].

The principal quantum number of ^{87}Rb is n= 5. The interaction of the spin of the valence electron $\vec{S}$ with the angular momentum of the whole atom $\vec{L}$ leads to the so called fine structure. The electron angular momentum is then given by $\vec{J} = \vec{S} + \vec{L}$, and therefore J can take the values 1/2 + $\{0,1,2,\cdots\}$ = $\{1/2,\ 3/2,\ 5/2,\ \cdots\}$. Taking into account the notation of the energy levels $n^{2S+1}L_J$, the ground state is $5^2\mathrm{S}_{1/2}$ (L=0) and the two following excited states are then $5^2\mathrm{P}_{1/2}$ and $5^2\mathrm{P}_{3/2}$ (L=1). The corresponding transition from the ground state to these excited states are called D_1 and D_2 lines respectively, and their wavelengths read 794.9788509(8) and 780.241209686(13) nm [11].

In turn, the coupling between the electron angular momentum $\vec{J}$ and the atom spin $\vec{I}$ gives rise to the hyperfine structure. Then, the total atom angular momentum is given by $\vec{F} = \vec{J} + \vec{I}$, and it lifts the degeneracy of the energy levels. In figure 2.1 is shown the

Basic properties	
Atomic mass m	86.909 180 520(15) u 1.443 160 60(11) $\times$ 10^{-25} kg
Melting point T_M	39.31 ^{o}C
Cycling transition properties	
Vacuum wavelength λ_0	780.241 209 686(13) nm
Frequency ω_0	$2\pi \cdot$ 384.230 484 468 5(62) THz
Linewidth Γ	$2\pi \cdot$ 6.065(9) MHz
Lifetime τ	26.14(4) ns
Recoil velocity v_r	5.8845 mm/s
Doppler Temperature T_D	146 μK

Table 2.1: Basic properties of ^{87}Rb.

structure of D_2 line of ^{87}Rb energy levels, where the degeneracy of the ground and the excited state can be observed.

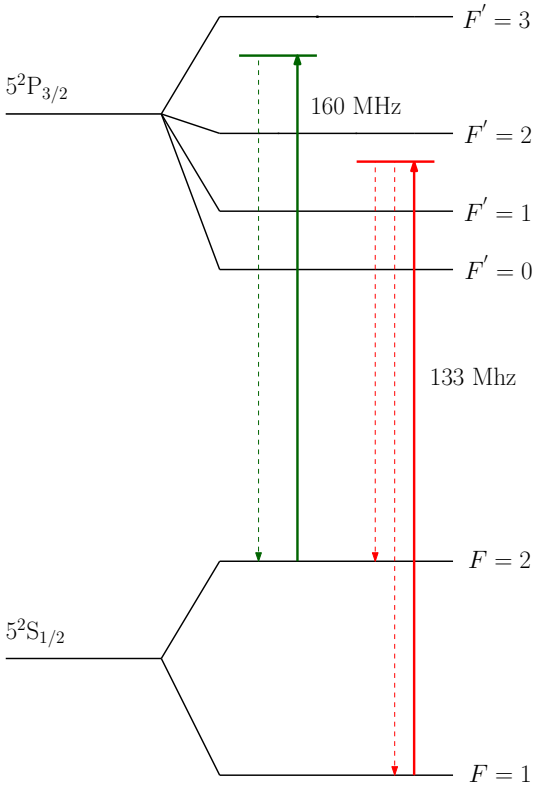

Figure 2.1: Energy levels of the D_2 atomic line transition of ^{87}Rb. The two employed transitions, cooler and repumper, are indicated in green and red color respectively. Dashed lines indicate the decays that may occur.

2.1.2 Laser sources

Consider an atom approximated to a two-level system, namely the ground state $|a\rangle$ and the excited state $|b\rangle$. Let me assume that the state of the atom, at a given time t, is localized in $|a\rangle$: if the atom absorbs a photon with frequency ω_{ab}, corresponding to the transition $|a\rangle \rightarrow |b\rangle$, then it is excited to $|b\rangle$. However, after a certain mean time τ the atom will re-emit the photon and will decay to the ground state. This time τ is called the decay lifetime, and it depends on the properties of the specific transition.

The $|F = 2\rangle \rightarrow |F^{'} = 3\rangle$ transition on the D_2 line (depicted in figure 2.1) is a closed transition, which means that the excited atom can only decay into the ground state. This makes it appropriate for laser cooling. However, there is a finite probability that some atoms are excited to $|F^{'} = 2\rangle$ state decaying then into $|F = 1\rangle$. So, to solve this problem, another frequency have to be add to drive these atoms to $|F = 2\rangle$. In this way, a closed circle is achieved and the atoms can be efficiently cooled down. The first frequency is called **cooler**, and it drives the mentioned transition $|F = 2\rangle \rightarrow |F^{'} = 3\rangle$. The second one is the **repumper**, which acts on the $|F = 1\rangle \rightarrow |F' = 2\rangle$ transition, and brings the atoms back to the cooling cycle. In figure 2.1 both transitions are shown with their respective decays.

2.1.3 Cooling, optical molasses

In order to cool down and trap the atoms two techniques must be used: optical molasses and magneto-optical traps.

The laser produces a well-collimated monochromatic beam of light that may slow down the atoms. Each absorbed photon gives the atom a kick in the opposite direction to its motion, emitting then photons in random directions. This scattering of many photons gives an average force that slow the atoms down [12].

The force, F_{sc}, which an atom feels because of the laser light scattering is given by

$$F_{sc} = \hbar k \frac{\Gamma}{2} \frac{I/I_{sat}}{1 + I/I_{sat} + 4\Delta^2/\Gamma^2}, \tag{2.1}$$

where I is the intensity of the light, I_{sat} is the saturation intensity, Γ is the lifetime, and Δ is the detuning, *i.e.* the difference between the frequency of the laser ω and the frequency of the transition ω_0.

In the optical **molasses technique** the Doppler effect plays an important role. An atom with a certain velocity v "sees" a different frequency of the laser interacting with it. So, the detuning results in $\Delta \rightarrow \Delta \pm kv$ depending on the sign of the direction of motion with respect to the laser beam. Considering only one dimension, that is, two beams propagating in opposite directions, the net force F_{mol} experienced by an atom is given by

$$F_{mol} = F_{sc}(\Delta - kv) - F_{sc}(\Delta + kv), \tag{2.2}$$

and assuming the condition $kv \ll \Delta$, then

$$F_{mol} \approx \left(F_{sc}(\Delta) - kv\frac{\partial F_{sc}}{\partial \omega} \right) - \left(F_{sc}(\Delta) + kv\frac{\partial F_{sc}}{\partial \omega} \right) = -2kv\frac{\partial F_{sc}}{\partial \omega}. \tag{2.3}$$

The last expression can be easily obtained from (2.1), and therefore

$$\frac{\partial F_{sc}}{\partial \omega} = -\hbar k \frac{4\Delta}{\Gamma} \frac{I/I_{sat}}{(1 + I/I_{sat} + 4\Delta^2/\Gamma^2)^2}, \tag{2.4}$$

which is positive when the laser is red-detuned, $\Delta < 0$, and negative otherwise. So, using a red-detuned laser beam, the force F_{mol} (2.1) has the opposite direction of the velocity of the atoms and, therefore, it cools them down.

2.1.4 Magneto-Optical Trap

In order to trap the atoms, the force experienced by the them has to depend on their position. The addition of a magnetic field satisfies this condition. The optical molasses configuration with the addition of a quadrupole magnetic field is called **magneto-optical trap**. This magnetic field causes an imbalance in the scattering forces of the laser beams and a strong atomic confinement is achieved through the radiation force [12]. Furthermore, this magnetic field also splits the F levels into the correspondent m_F sublevels (Zeeman effect).

The principle of the MOT is illustrated in figure 2.2 for the $|F = 2\rangle$ to $|F' = 3\rangle$ transition. In the center of the trap the magnetic fields produced by the coils cancel out, so that $B = 0$. In that region, there is a constant magnetic field gradient which perturbs the energy levels; the Zeeman effect causes the energy splitting of the 7 sublevels in the $F' = 3$ state and 5 sublevels for $F = 2$, which depends linearly on the position of the atom. Moreover, the polarization of the light now plays an important role. The right-handed polarized beam σ^+ propagates in $+\vec{z}$ direction, and the left-handed polarized beam σ^- in $-\vec{z}$ direction. According to the angular momentum conservation rules, the σ^+ light can only excite electrons from m_F to $m_{F'} + 1$. In the other case, the transition has to be from m_F to $m_{F'} - 1$. Because of this fact, the Zeeman effect changes the transition frequency from ω_0 to $\omega_0 \pm \beta z$, depending on the polarization of the light.

To describe the magneto-optical trap mathematically we can add the frequency shift produced by the Zeeman effect to equation (2.2)

$$F_{MOT} = F_{sc}^{\sigma^+}(\Delta - kv - \beta z) - F_{sc}^{\sigma^-}(\Delta + kv + \beta z), \tag{2.5}$$

and considering $kv + \beta z \ll \Delta$ then

$$F_{MOT} = -2(kv + \beta z)\frac{\partial F}{\partial \omega}, \tag{2.6}$$

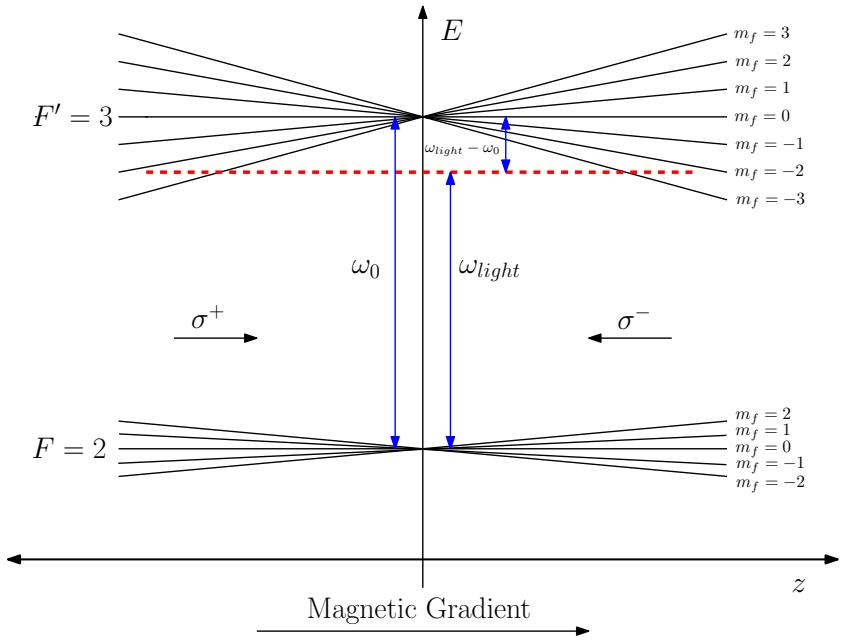

Figure 2.2: Working principle of the MOT for ^{87}Rb atoms.

where β is a coefficient proportional to the magnetic field.

As one can see, this result is quite similar to (2.3) with an additional term. Molasses only cool the atoms while MOT cools and traps. The force of the molasess only depends on v. The force of the MOT depends on v and z, which provides a spatial confinement. Nevertheless, Zeeman effect makes the cooling less effective, therefore the optical molasses technique is required to be employed after the MOT step. However, the minimum temperature that can be reached through this technique is 140 μK for Rubidium, hence it is insufficient to reach the BEC state. The following technique, called dipole trap, allows a further cooling down.

2.1.5 Dipole Trap

The experimental realisation of Bose-Einstein condensation requires increasing the phase-space density PSD= $n\lambda_{\text{th}}^3$ to values closer to 1 [13], where n is the density of atoms and

$$\lambda_{\text{th}} = \sqrt{\frac{h^2}{2\pi m k_B T}}. \tag{2.7}$$

After the atoms have been cooled and trapped the PSD has a value approximately of 7 x 10^{-8} [1], so it is still necessary to increase the PSD by several orders of magnitude to reach Bose-Einstein condensate state. To achieve it, we use the evaporative cooling method.

Dipole traps allow us to implement this technique in the experiment. This cooling technique gets lower temperatures than the previous method, making possible the condensation. This mechanism is analogous to what happens in a cup of tea: the hottest

atoms, the ones with higher velocities, can escape from the trap lowering the average temperature of the remaining ones. Ramping down slowly the trap depth, the temperature is lowered down. In figure 2.3 it is shown a schematic representation of this procedure. This method is used after the MOT stage in order to reach the Bose-Einstein Condensation.

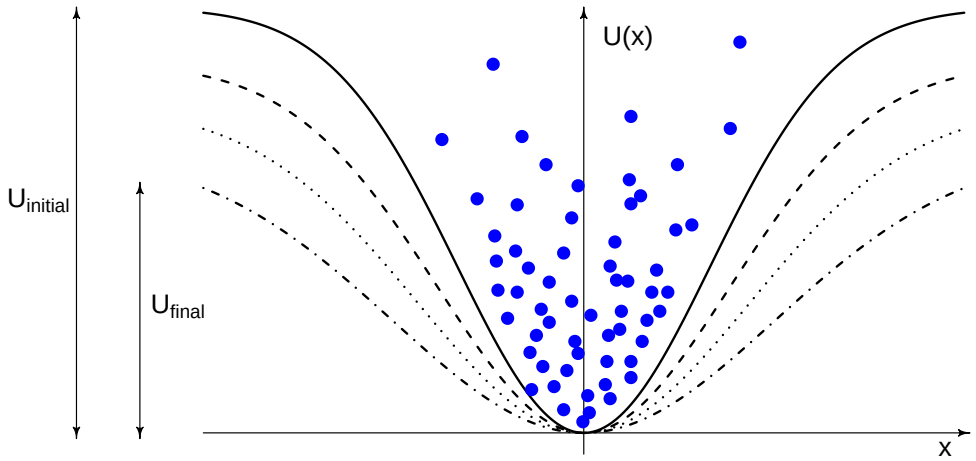

Figure 2.3: Scheme of evaporation from a dipole trap.

A common way to create a dipole trap with 3-dimensional confinement consists in using a far-detuned gaussian beam. The optical dipole force arises from the reactive interaction between the induced atomic dipole moment with the intensity gradient of the light field. Since it is a conservative force, it can be derived from a potential, the minima of which can be used for atom trapping. The interaction potential of the induced dipole moment $\vec{p}$ in the driving field $\vec{E}$ is given by [14]

$$U_{\text{dip}}(\vec{r}) = -\frac{1}{2}\langle \vec{p}\vec{E}\rangle = -\frac{1}{2\epsilon_0 c}\text{Re}(\alpha)I(\vec{r}), \tag{2.8}$$

where α is the polarizability, and the field intensity reads $I = 2\epsilon_0 c|E|^2$. The factor $1/2$ is due the fact that the the dipole moment is induced, not permanent. Then, the dipole force results from the gradient of the interaction potential

$$\vec{F}_{\text{dip}}(\vec{r}) = -\nabla U_{\text{dip}}(\vec{r}) = \frac{1}{2\epsilon_0 c}\text{Re}(\alpha)\nabla I(\vec{r}). \tag{2.9}$$

On the other hand, the power absorbed by the atoms depends on the imaginary part of the polarizability. The corresponding scattering rate is

$$\Gamma_{\text{sc}}(\vec{r}) = \frac{1}{\hbar\epsilon_0 c}\text{Im}(\alpha)I(\vec{r}). \tag{2.10}$$

Since the Rubidium has a complex hyperfine structure, in order to compute the po-

tential created by the laser beam it is necessary to consider the contribution of the polarizability from both D_1 and D_2 transitions. Therefore, the dipole potential and the scattering rate are given by [14]

$$U_{\mathrm{d}}(\vec{r}) = \frac{\pi c^2 \Gamma}{2\omega_0^3}\left(\frac{2+\mathscr{P} g_F m_F}{\Delta_{D2}} + \frac{1-\mathscr{P} g_F m_F}{\Delta_{D1}}\right) I(\vec{r}), \tag{2.11}$$

$$\Gamma_{\mathrm{sc}}(\vec{r}) = \frac{\pi c^2 \Gamma^2}{2\hbar\omega_0^3}\left(\frac{2}{\Delta_{D2}^2} + \frac{1}{\Delta_{D1}^2}\right) I(\vec{r}), \tag{2.12}$$

where g_F is the Landé factor, $\Delta_{Di} = \omega_i - \omega$ are the energies splittings of the D_1 and D_2 lines, and $\mathscr{P}$ is the polarization of the light. If the laser is linearly polarized (represented as π) $\mathscr{P} = 0$ but if it is circularly polarized ($\sigma^{\pm}$) then $\mathscr{P} = \pm 1$. The two terms between parentheses in equation (2.11) represent the contributions of the $D1$ and $D2$ lines to the total dipole potential. An important thing to mention is that the scaling laws of the potential and the scattering rate are

$$U_{\mathrm{d}} \propto \frac{I}{\Delta} \quad \text{and} \quad \Gamma_{sc} \propto \frac{I}{\Delta^2}. \tag{2.13}$$

Therefore, optical dipole traps usually use large detunings and high intensities in order to keep the scattering rate as low as possible, since scattering is a heating mechanism.

Gaussian beams

In the experiment, dipole trap is generated by the crossing of two far-detuned gaussian lasers of 1550nm and 1070nm of wavelength. The combination of these two beams into a crossed dipole trap allows to cool down the atoms from 150 μK to $\sim$20 nK, and to increase the phase space density of our sample. This makes possible to reach the Bose-Einstein condensation phase within few seconds, as I will describe later.

The spatial intensity distribution of a focused Gaussian beam with power P which propagates along the z-axis is described by

$$I(\vec{r}) = \frac{2P}{\pi w(z)} \exp\left(-\frac{2\rho^2}{w^2(z)}\right), \tag{2.14}$$

where $\rho^2 = x^2 + y^2$, z denotes the direction of the propagation. The $1/e^2$ radius $w(z)$ depends of the axial coordinate via z

$$w(z) = w_0\sqrt{1 + \frac{z}{z_R}}, \tag{2.15}$$

where the minimum radius w_0 is commonly called the beam waist and $z_R = \pi w_0^2/\lambda$ is the Rayleigh length.

Therefore, the dipole potential performed in the experiment is proportional to

$$U_{\mathrm{d}} \propto \frac{2P_{1070}}{\pi\omega_{1070}(z)} \exp\left(-\frac{2\rho^2}{\omega_{1070}^2(z)}\right) + \frac{2P_{1550}}{\pi\omega_{1550}(z)} \exp\left(-\frac{2\rho'^2}{\omega_{1550}^2(z)}\right), \tag{2.16}$$

with $\rho'^2 = x'^2 + y'^2$ and $x' = x\cos\theta - y\sin\theta, y' = x\sin\theta + y\cos\theta$, where θ is the angle of the cross. When the energy of the atomic ensemble k_BT is much smaller than the depth of the potential $U_0 = U(\vec{r} = \vec{0})$, then the dipole potential can be approximated by a harmonic potential given by,

$$U_{\mathrm{d}} \approx U_0 + \frac{1}{2}m(\omega_x^2x^2 + \omega_y^2y^2 + \omega_z^2z^2). \tag{2.17}$$

The frequencies ω_i, $i = x, y, z$ are the so-called trapping frequencies, and we can theoretically compute them by

$$\omega_x = \sqrt{\frac{2}{m}\frac{\partial U_{\mathrm{d}}}{\partial x}\bigg|_{\vec{r}=\vec{0}}}, \quad \omega_y = \sqrt{\frac{2}{m}\frac{\partial U_{\mathrm{d}}}{\partial y}\bigg|_{\vec{r}=\vec{0}}}, \quad \omega_z = \sqrt{\frac{2}{m}\frac{\partial U_{\mathrm{d}}}{\partial z}\bigg|_{\vec{r}=\vec{0}}}. \tag{2.18}$$

2.2 Experimental sequence

As introduced before, a BEC experiment involves several lasers, and each of them requires a control of frequencies and powers. To do that, a sophisticated computer control system is required. Cicero Word Generator is the software used to implement the sequence to run the experiment. It allows us to define how the different required channels have to work, including complex signals which follow different patterns of intensity. We employ a total number of 7 analog and 14 digital channels.

In figure 2.4 I present a schematic representation of the experimental sequence. The atoms are initially loaded in the 2D Magneto-Optical Trap (MOT) chamber where are pushed to the science chamber. There, they are cooled using standard laser cooling techniques to approximately 150 μK in a 3D MOT (steps: *Loading MOT - Dark MOT*). After that, the atoms are transferred to an optical dipole trap where the condensation is achieved by evaporative cooling (steps: *Ramp 1 - Ramp 7*). In order to collect the data, absorption imaging technique is used as final step (*Imaging*). *TOF* means "time of flight", and it is the time in which the sample evolves when the dipole trap is off. In this section, I will explain these stages step by step. In figure 2.5 is shown a screen-shot of Cicero with the standard sequences designed for the experiment.

In order to analyse the data, two programs written in Python are used: *Acquire* and *Cam Strip Down*. The first one enables the camera-computer connection and processes the pictures taken with the camera. The second one allows us to fit the data as I will explain at the end of this chapter. I improved this last program by adding some new features. It initially provided only one screen to make the analysis, and I improved it by

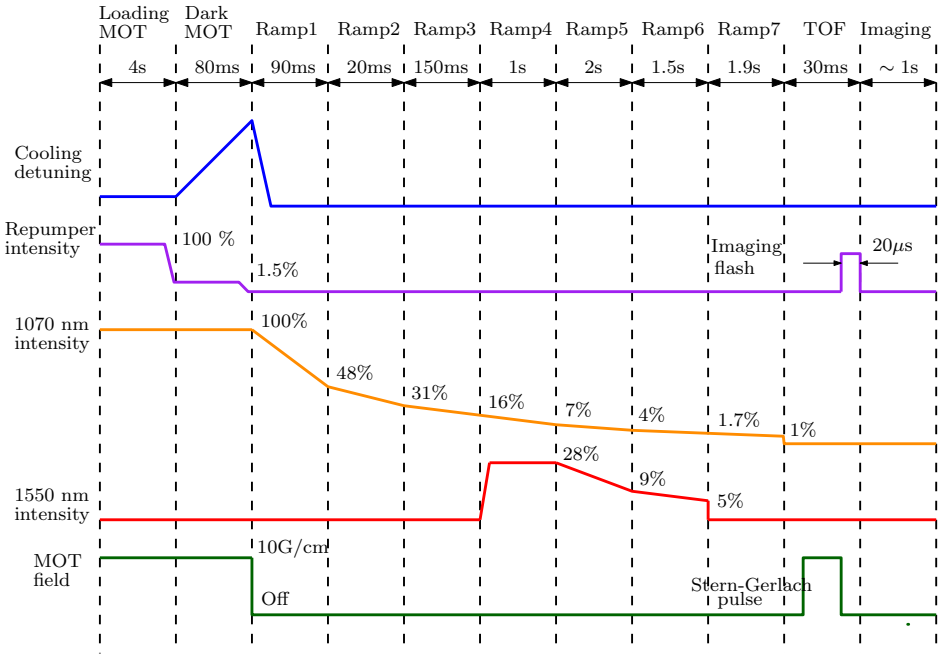

Figure 2.4: Schematic sequence required to get the condensate in our experiment [1]. It is divided in steps which are the different stages implemented in the software.

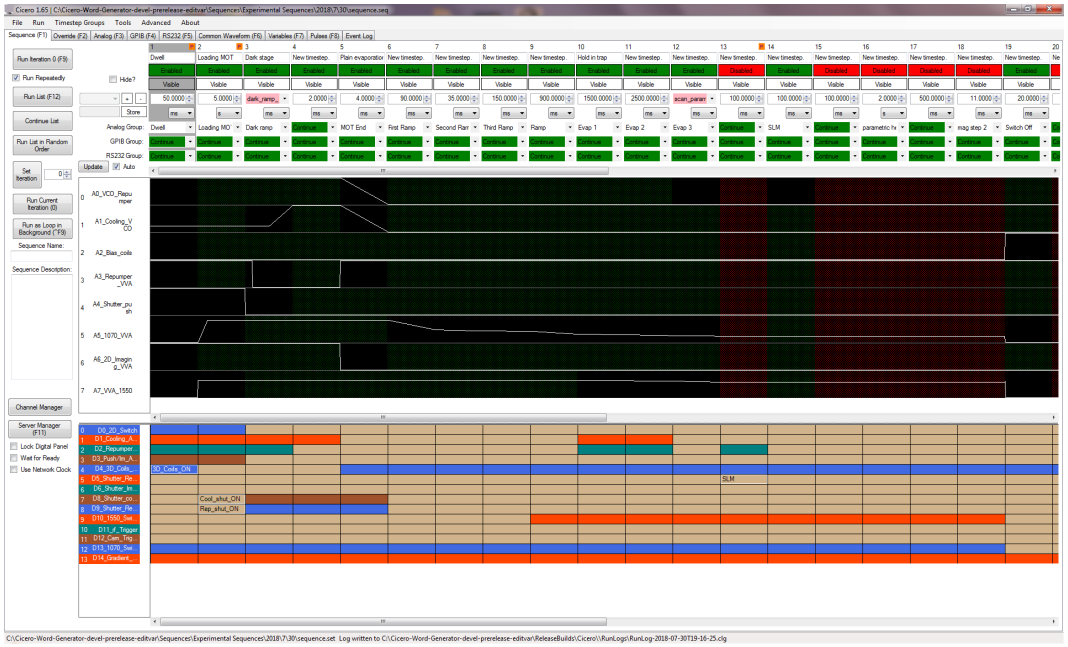

Figure 2.5: Screen-shot of Cicero where the different time stages can be seen on top. Under these, the different functions of the analog channels are implemented. The digital channels are located in the bottom part, where a colored square means state on.

adding two other independent screens. This is an efficient and helpful tool, since we can image the three Zeeman states by Stern-Gerlach method and analyse them independently. In subsequent sections, I will discuss this method more in depth.

After having applied absorption imaging, the atomic cloud does not exist anymore, which means that every sequence produces a sample under certain conditions. So, when we want to collect data, we need to run several sequences changing the control parameters each time. Cicero can create a list of different values associated to one of the defined variables and it will be iterating that list before running. To get a good statistic, several sequences have to be executed with the same control parameters.

2.2.1 2D MOT

The vacuum system is divided in two main chambers, 2D MOT and 3D MOT chambers, separated by a differential pumping stage which allows for a pressure difference of the order of $\sim 10^3$. Thanks to this, we can keep a lower a pressure in the 3D MOT, in the order of $\sim 10^{-10}$ mbar, avoiding the excess of background collisions that otherwise would destroy the BEC while keeping the pressure in the 2D MOT chamber in the order of that of the Rb vapor pressure at room temperature ($\sim 10^{-7}$ mbar). This allows us to generate a stream of cold atoms towards the 3D MOT providing $\sim 10^9$ atoms in this one in a loading time of 4 s.

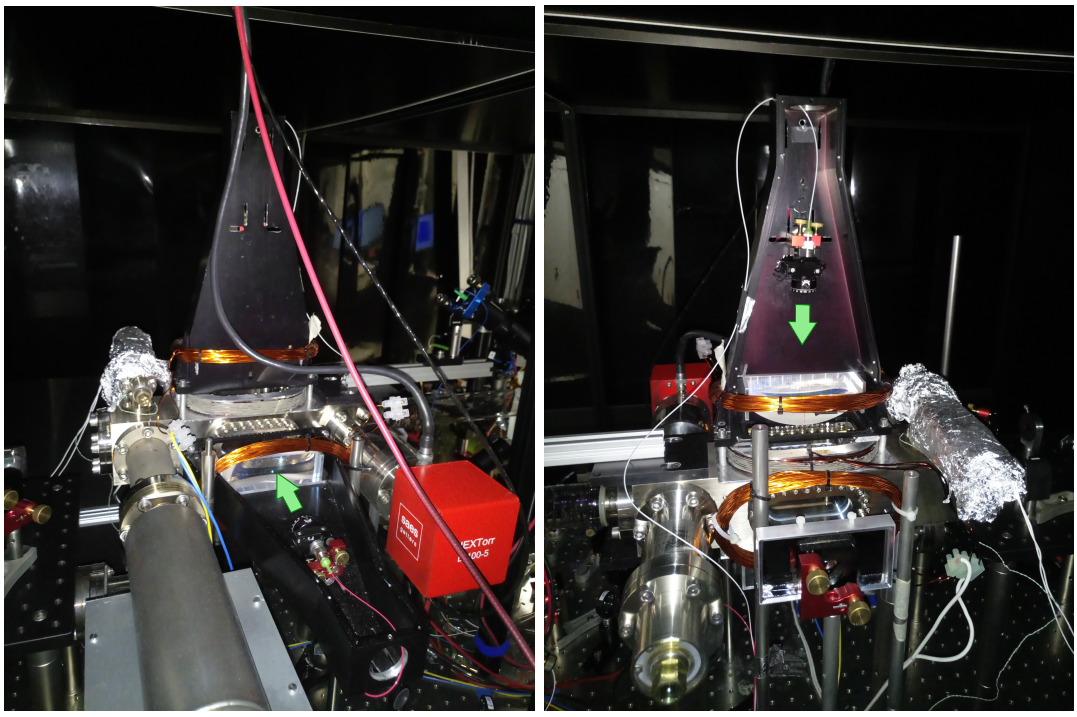

(a) (b)

Figure 2.6: Two perspectives of the 2-Dimensional Magneto-Optical Trap. The laser confinement is given by the orthogonal crossing of two beams and their respective reflections provided by a mirror. The green arrows represent the direction of propagation of the beams.

The experiment starts in the chamber of the 2D MOT, where the atoms are loaded from the vapor. The 2D MOT consists of two perpendicular counterpropagating beams and two pairs of coils in anti-Helmholtz configuration, which provide a 2-dimensional atomic confinement. The magnetic field gradient created in the center of the chamber is 10 G/cm. The light delivered to the chamber contains both cooler and repumper frequencies. The powers of the cooling and repumper lasers are 50 and 20 mW per beam, respectively. In the figure 2.6 is shown the 2D MOT from two perspectives.

In order to transfer the atoms to the science cell, they are pushed by the **push beam**. This beam is a linearly polarized beam with 1.5 mW of power.

2.2.2 3D MOT

Set-up

The 3D MOT is created by three counterpropagating beams, providing a strong 3-dimensional confinement. The coils in anti-Helmholtz configuration produce a magnetic quadrupole with a gradient of 10 G/cm in the center. Another pair of coils in Helmholtz configuration is placed along the vertical direction in order to correct the residual magnetic field. The power of the cooler reads 15 mW per beam and 8 mW in total for the repumper. The later is provided only in one direction.

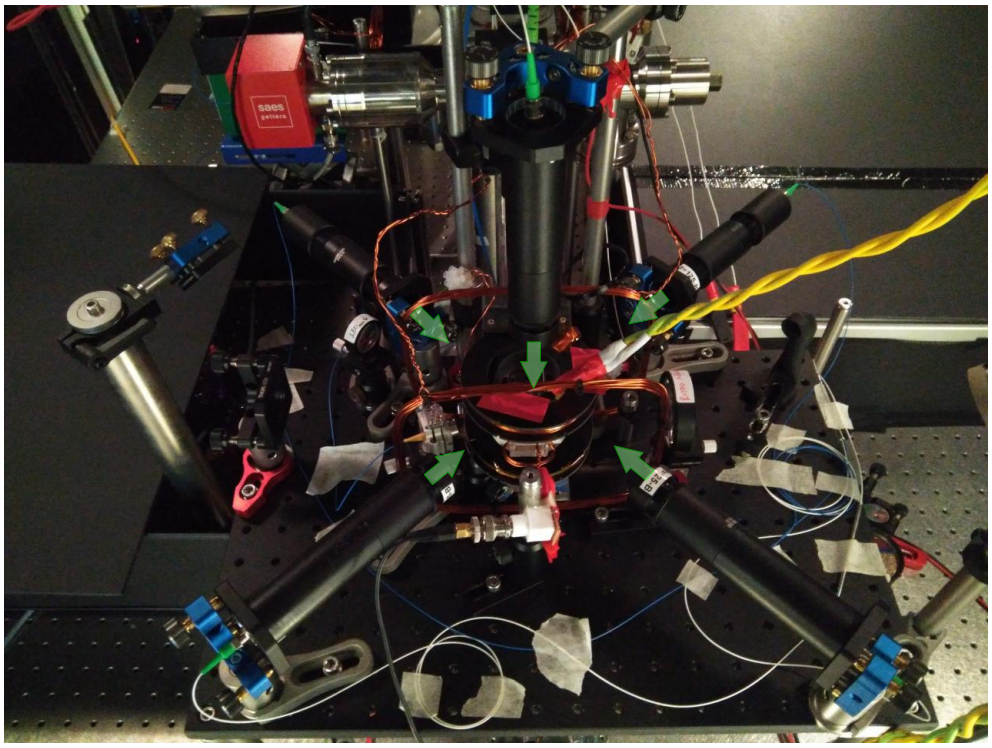

Figure 2.7: Previous configuration of the 3D MOT: 3 pairs of mutually orthogonal beams and a pair of coils in the vertical direction. The green arrows represents the direction of propagation of the beams.

One of the changes that I have done in the experimental set-up consists in rotating the 3D MOT. This new configuration allows to build the phase-imprinting apparatus, which will be discussed in the next chapter. In figures 2.7 and 2.8, it can be seen the previous and the current configuration of the 3D MOT, respectively. The change consists of a rotation of 90° of the complete set-up. In the former scheme, four beams crossing in the radial direction were orthogonal, while now two pairs cross at 60°. This provides better optical access in the vertical direction and makes space for the objectives needed to perform phase-imprinting. After a few initial tests, a new pair of coils were necessary in the vertical axis for the compensation of residual magnetic fields and, in the end, in order to trap more number of atoms.

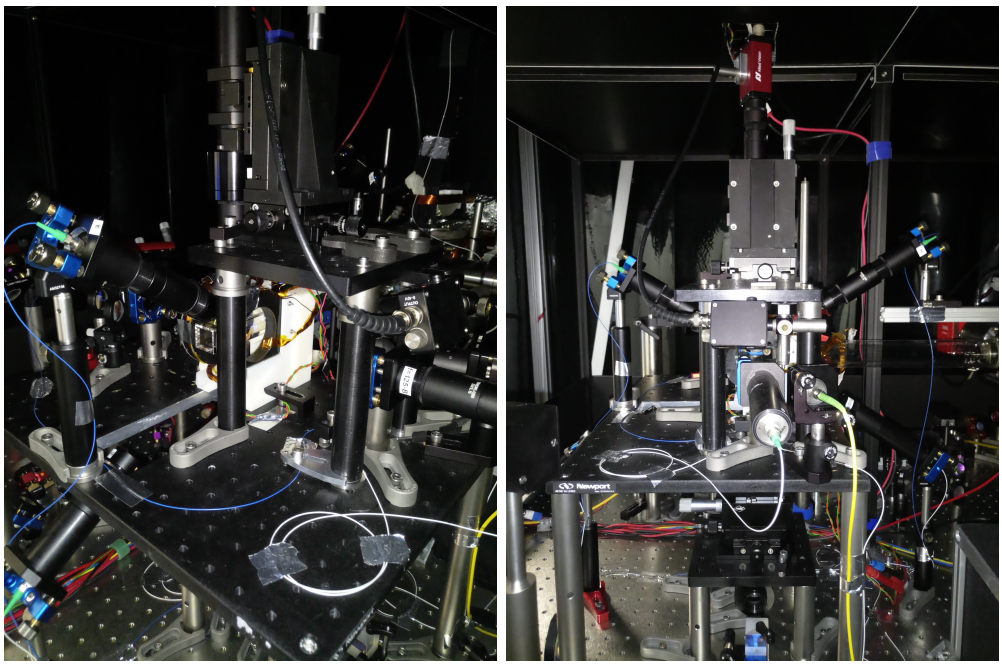

(a) (b)

Figure 2.8: Current configuration of the 3D MOT: 2 pairs of counterpropagating beams with a crossing of 60º, another counterpropagating beam perpendicular to them, and a pair of coils in the horizontal direction.

Implementation of the 3D MOT

After 5 seconds of loading, the temperature of the sample is 150 μK. To effectively load the dipole trap, one needs to lower the temperature of the atoms even more. To do this we apply a technique called **Dark MOT**. During this stage, we further detune the cooler laser about 80 MHz fromm resonance, and lower the intensity of the repumper laser during 80 μs. As mentioned before, the cooling force depends on the detuning Δ (equation (2.1)). Then, the atoms are forced to remain in $|F = 1\rangle$ state. As a result of this technique, the temperature of the atomic cloud is near 50 μK and the number of atoms is 10^8. Then, the system is ready to start with the evaporative cooling. In figure 2.9, I present a picture of the atoms trapped in the 3D MOT.

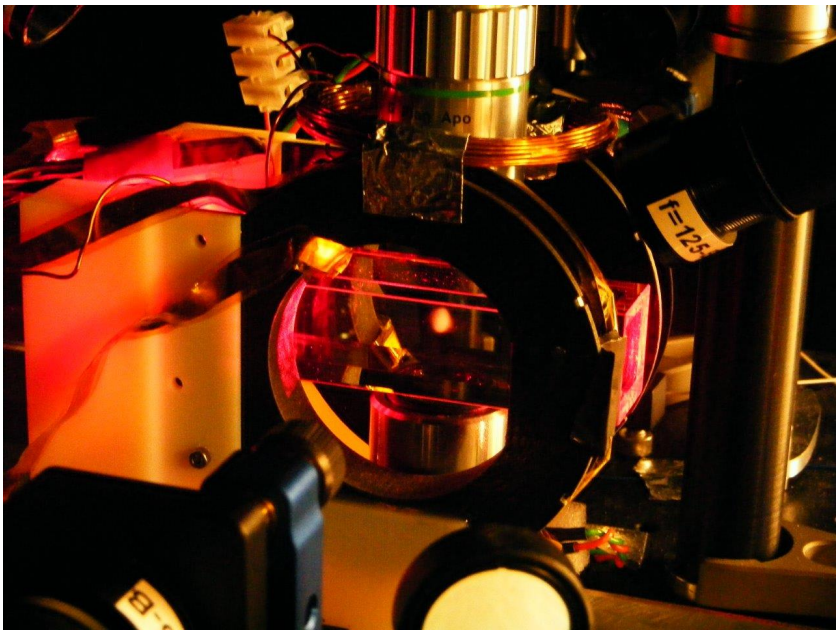

Figure 2.9: Atoms trapped in the 3-Dimensional Magneto-Optical Trap.

2.2.3 Evaporative cooling

In this experiment, we perform evaporative cooling using all-optical methods. This technique was first used by Barret [15]. Essentially, evaporation relies on exponentially lowering the depth of the trap, removing in that way the hottest atoms, and waiting for a time long enough to let the trapped atoms thermalise. With this method, lower temperatures are achieved as a consequence of losing the hottest atoms.

Set-up

Our dipole trap consists of two far-detuned, gaussian beam at 1070 nm and 1550 nm. The 1070 nm one is an industrial standard multimode laser with a total output of 21 W. The 1550 nm one has an output of 25 mW reaching a total power of 8 W after amplification. Both lasers are sent to the science cell following free-space optical path, and are focused in the center of the 3D MOT. In this position, the 1070 nm laser has a waist of approximately 33 μm, and the 1550 nm has a waist of 40 μm. In figure 2.10 is shown the schematics of these optical systems including the sizes of the waist in each section of the trajectory, as well as the magnifications factors of the telescopes used.

In the picture also appears another important device: the Acousto-Optical Modulator (AOM). This useful device essentially allows the frequency, intensity, and direction of the laser to be modulated. It has two purposes: to control the intensity of the incoming laser and to allow the quick switching of the beam. The AOM diffracts the incoming light into several orders, and it is aligned in such a way that the output consists of the zeroth and the first orders, maximising the power of the last one. After the AOM, we put a beam blocker to block the zeroth order. To make the AOM work, it requires three components: a Voltage Controlled Oscillator (VCO), a Voltage Variable Attenuator (VVA), and an

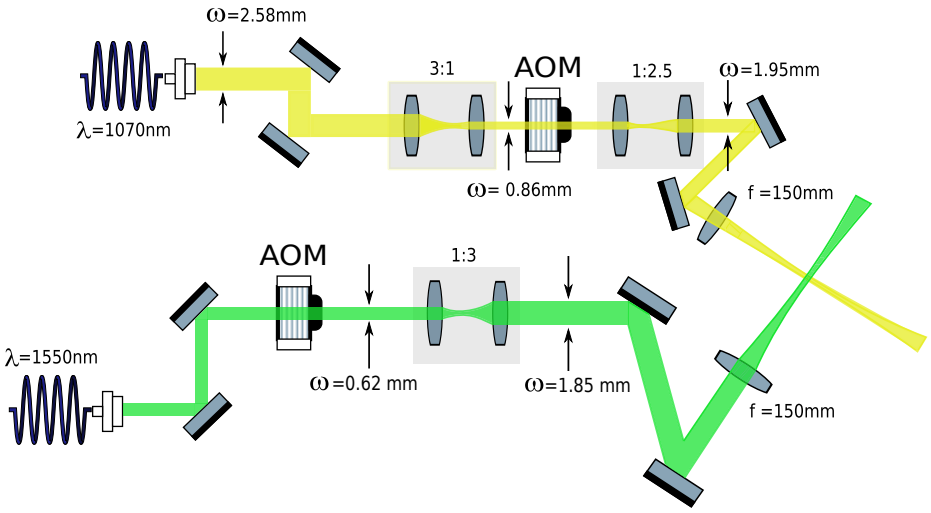

Figure 2.10: Schematic diagram (not to scale) of the dipole trap.

amplifier. The VCO fixes the frequency of the circuit, the VVA controls the power of the diffracted first order of the input light, and the amplifier amplifies the output of the VVA. In figure 2.11, I show how these components have to be connected. We also place a switch after the VVA to enable the mentioned quick switching of the beam.

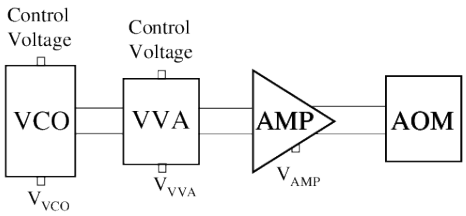

Figure 2.11: Schematic diagram showing how the VCO, VVA and amplifier are connected to the AOM [2].

Furthermore, I also made some changes in the optical system of both 1070 nm and 1550 nm lasers. Previously, the 1550 nm laser was sent to the experiment, after the AOM, by fiber coupling using a high power coupler. As time went on, I saw how this set-up was losing efficiency. So now, this laser is delivered by free-space optics as shown in figure 2.10. It is sent to the AOM in a single pass-configuration and then is magnified by a 1:3 telescope made by two achromatic lenses, f=100 mm and f=300 mm. Finally, the beam is sent to the science cell using a periscope with high precision mirror mount alignment. Another lens with f=150mm is placed before the cell to focus the beam in the center with a waist of 40 μm. With this configuration more power than before is available, approximately 5 W, much more than the experimental requirements.

Regarding the 1070 nm laser, it is sent to the experiment in a free-space configuration,

being first demagnified (3:1) before the AOM and second magnified (1:2.5) after. The first telescope is made of two achromatic lenses of f=50 mm and f=150 mm, while the second one is made of f=100 mm and f=250 mm lenses. This beam also goes through the AOM in a single pass configuration. Similarly, the beam is sent to a science cell by a periscope with a high precision mirror mount, and another lens f=150 mm is used to focus it with a waist of 33 μm in the center. In the figure 2.12, I present a picture of this optical system. In the lower left corner, one can see the output of the 1070 nm laser, and in the right part, the periscope is placed.

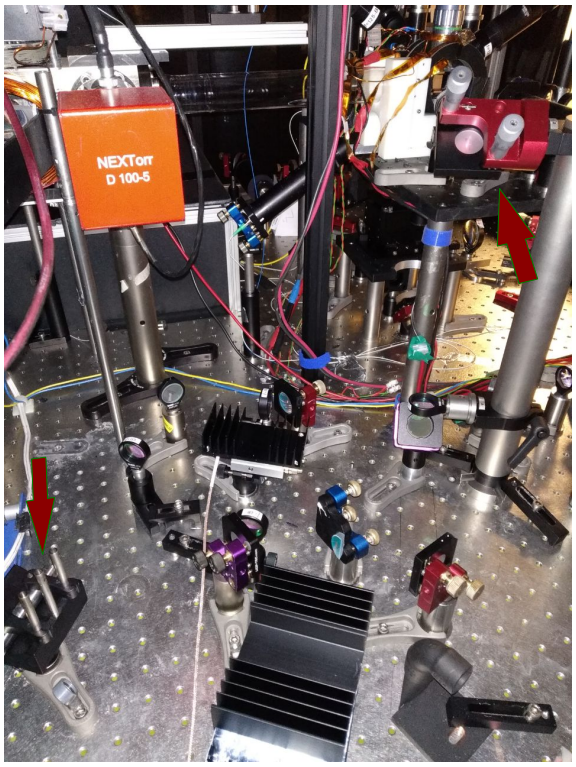

Figure 2.12: Free-space configuration of the 1070 nm laser. On the left, one can see the laser output. On the right, the periscope is placed and sends the beam to the science cell.

Implementation of the dipole trap

During the loading of the MOT, the 1070 nm laser is kept at 12 W, the maximum power that can be sent to the experiment. After the Dark MOT stage, the evaporation in 1070 trap starts. The ramp consists of an exponential ramp down during 1.2 seconds. Then, the 1550 nm laser is switched on with a power of 1 W, allowing to load colder atoms to this trap. In the end, the dipole trap achieves to cool down the atoms to 20 nK. This makes it possible to reach the condensation state.

Before the 1550 nm laser is switched on, the power of the 1070 nm one is decreased from 100% to 7% in four linear ramps. This is shown in figure 2.4. At this moment, the 1550 nm laser is switched on with a 28% of the total power available, which corresponds to 1.2W. Simultaneously, the power of the other one has been decreased to 4%. This step

is followed by other 2 linear ramps where the power of the 1550 nm and 1070 nm laser reach the 5% and 1%, respectively. In other words, 30 mW and 70 mW approximately. In figure 2.13 is shown the diople potential at the end of the evaporative cooling step.

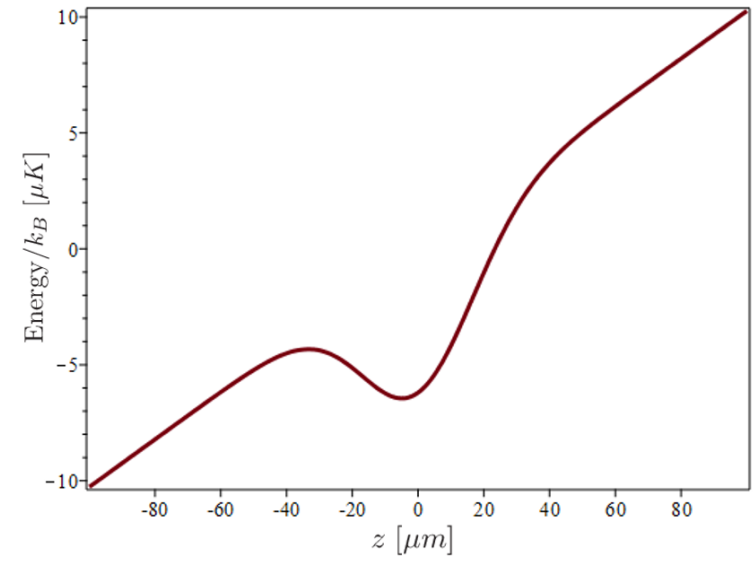

(a)

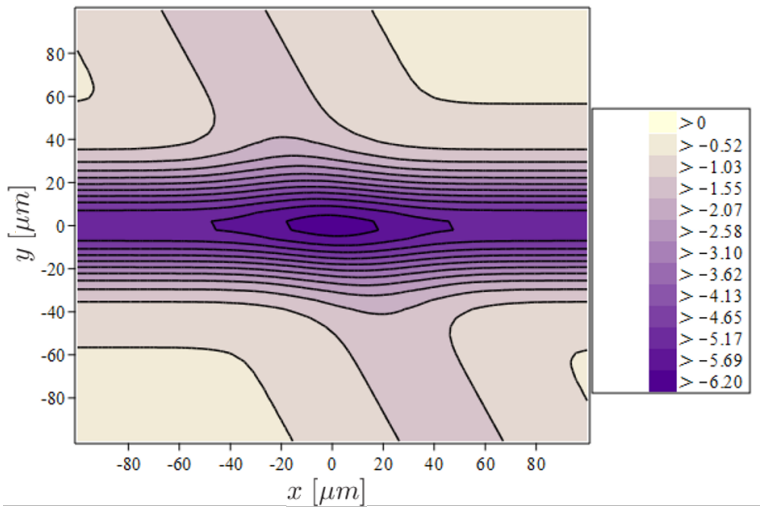

(b)

Figure 2.13: Representation of the dipole trap at the end of the evaporative cooling stage. Figure (a) shows the trap depth taking into account the effect of gravity, as a function of the distance z. The trap depth is 2.12 μK. In figure (b) shows the equipotential contour lines of trap in the horizontal plane xy for $z = 0$. The values of the waist and power are the ones mentioned in the text: $w_0 = 40\mu$m and $P = 30$mW for 1550 mm laser; and $w_0 = 30\mu$m and $P = 70$mW for 1070 mm laser. The potential is shown in terms of Energy/k_B in units of μK, where k_B is the Boltzmann constant.

After 6.5 seconds of total evaporation time, the result is a pure Bose-Einstein condensate of 10^5 atoms in the $|F = 1\rangle$. In figure 2.14(a) is shown a typical BEC after 30 ms of time of flight. The time of flight is the time needed for the sample to evolve without the

dipole trap and reduces the optical density. Initially, the cloud is much too dense, making impossible to take data.

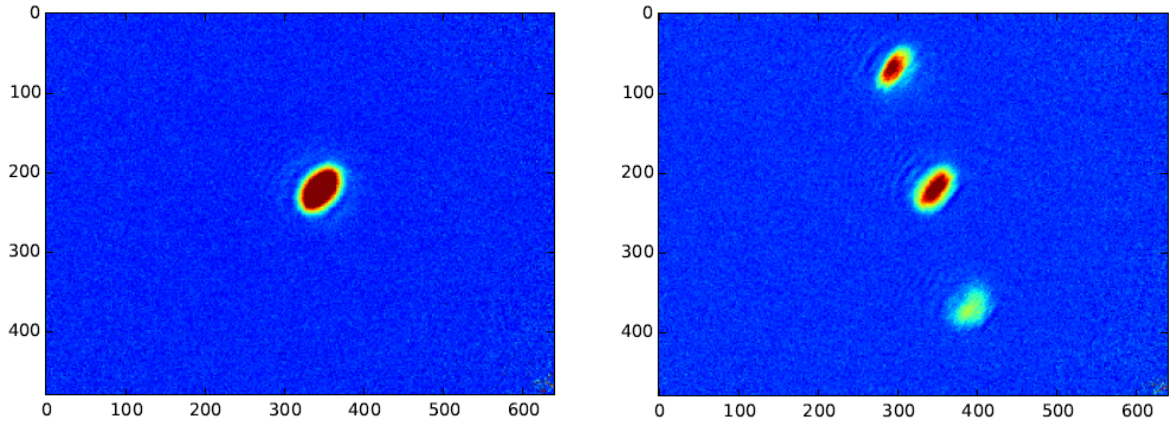

(a) (b)

Figure 2.14: Purely condensed Bose-Einstein Condensate after 30ms of time of flight.

An useful technique called Stern-Gerlach allows the separation of the clouds to display the Zeeman states independently. This method consists in switching on the MOT coils during the time of flight. This magnetic pulse generates a force which depends on the magnetic substates, m_F of each atom and the field gradient, and separates the cloud. A typical configuration is shown in figure 2.14(b).

2.2.4 Detection

Absorption imaging is the method used to obtain the density profile of the atomic cloud. The imaging laser used consists in a collimated beam with a frequency resonant with the transition $|F = 2\rangle \rightarrow |F' = 3\rangle$ on the D_2 line of the ^{87}Rb. At the end of the sequence, the atoms are in the $|F = 1\rangle$ state, so a flash of 15 μs of repumper light is required to repump to $|F = 2\rangle$ before taking the picture. The atoms absorb the light, leaving a shadow in the beam intensity distribution. The amount of light absorbed by the atoms is given by the Beer-Lambert law [16]

$$I = I_0 \exp\left(- \int n(z)\sigma dz \right), \tag{2.19}$$

where z is the direction of propagation of the beam, $n(z)$ the density of the atomic cloud, I_0 is the intensity of the beam, and σ is the absorption cross section of the atoms. We take three pictures in each experimental sequence. The first one is the picture of the imaging beam with atoms (I_1), the second one is the picture of the imaging beam alone (I_2), and, finally, the last picture is the background (I_3). Then, the column density of the atomic

cloud pixel by pixel is calculated according to [16]

$$\Omega(x,y) = -\log\left(\frac{I(x,y)}{I_0(x,y)}\right) = -\log\left(\frac{I_1(x,y)-I_3(x,y)}{I_2(x,y)-I_3(x,y)}\right). \tag{2.20}$$

Using this technique one may extract the spatial distribution of the optical density Ω of the sample since it is related to the density distribution of the atoms. All relevant physical parameters of the system are then obtained performing 2D robust non-linear fits to the optical density profile.

As I mentioned before, in order to analyse the data, two programs are used. The first one is *Acquire* which creates the computer-camera connection and processes the three taken pictures. Then, the result is given by (2.20) is sent to *Cam Strip Down*, where the data are fitted. In figure 2.15, a screen-shot of the program is shown. The corresponding fit that has to be used depends on the experimental conditions. In this picture, one can see the three independent screens which provide a very efficient way to extract the data.

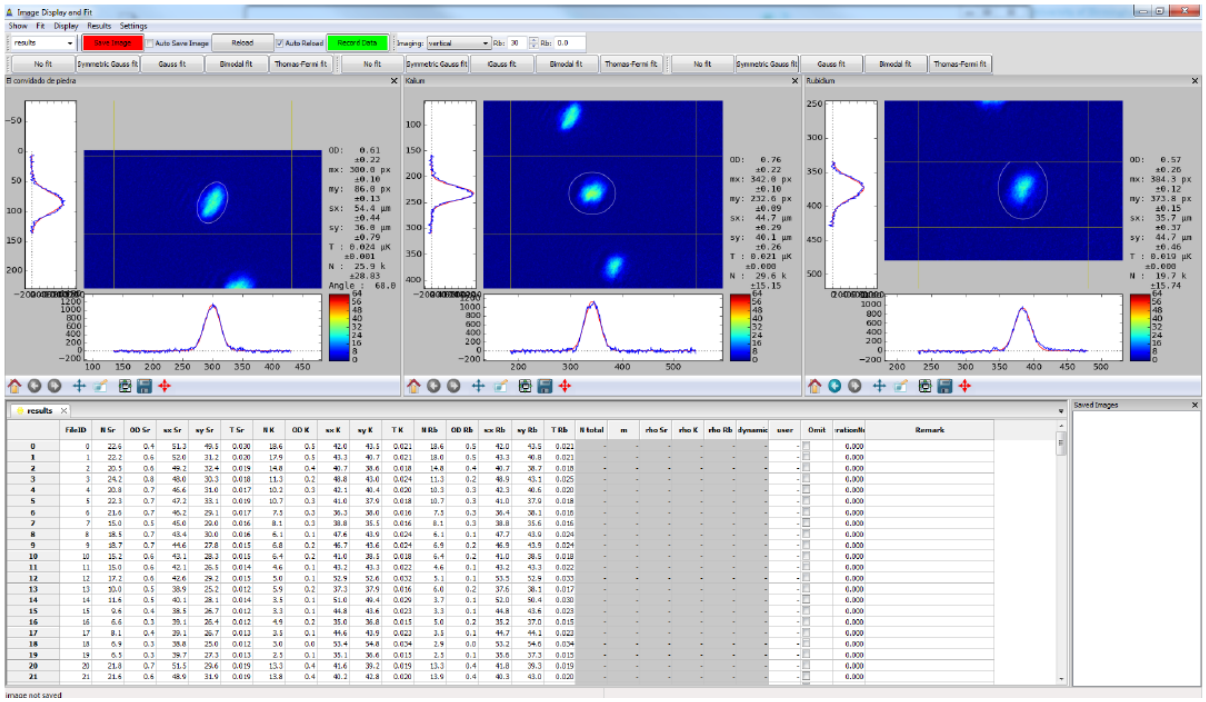

Figure 2.15: Screen-shot of *Cam Strip Down* for an experiment where three different atomic clouds coexist. Once they have been fitted, the density profiles and relevant parameters are shown.

1. If the temperature of the atoms is higher than the critical temperature, the density profile is expected to be a gaussian distribution

$$\Omega(x,y) = \frac{N\sigma_0}{2\pi\sigma_x\sigma_y}\exp\left(-\frac{(x-x_0)^2}{2\sigma_x^2}-\frac{(y-y_0)^2}{2\sigma_y^2}\right), \tag{2.21}$$

where N is the total number of atoms and σ_i are the widths of the cloud. On the other hand, the width of the sample depends of the temperature of the atoms in the following way

$$\sigma(tof) = \sigma(0)^2 + \frac{tof^2 T k_B}{m} \approx \frac{tof^2 T k_B}{m}, \tag{2.22}$$

where T is the temperature in the initial time, k_B is the Boltzmann constant, m is the mass of the ^{87}Rb atom, and it is being assumed that the cloud size is initially very small compared to the cloud after the time of flight, tof. So, applying the equation (2.22) the temperature of the sample is known.

2. If the temperature of the system is much lower than the critical temperature, all the atoms are condensed by definition. In this case, the profile of the cloud can be approximated by the Tomas-Fermi equation, given by

$$\Omega(x, y) = \frac{5N}{2\pi r_x r_y} \max\left(1 - \frac{(x - x_0)^2}{r_x^2} - \frac{(y - y_0)^2}{r_y^2}, 0\right)^{3/2}, \tag{2.23}$$

3. Finally, if the temperature is closer to the critical point, the cloud presents both a condensate part and a thermal part. This means that the profile is fitted as a combination of (2.21) and (2.23).

When the fits are done, all the involved parameters are saved and collected in a table. This table can be seen in figure 2.15. The program also permits the implementation of customized expressions which are shown and can be plotted in real time. This tool allows a faster and easier analysis of the measurements before the proper one.

Chapter 3

Phase-imprinting set-up

In the previous chapter, I have described the experimental set-up and how it works. In contrast, in this chapter, I will describe the new element added to the experiment. It is an opto-electronic system which allows the application of the phase-imprinting technique on the condensate. This technique is based on the imposition of phase profiles on the condensate which allows the creation of different topological states such as vortices or solitons.

The opto-electronic system consists of two elements. The first element is the spatial light modulator (SLM), which allows us to create different kind of light patterns when it receives a light beam. The second one is a microscope objective which demagnifies the pattern to be of the order of the atom cloud ($\sim 60\mu$m), and focuses it on the atom plane. In the following sections, I will explain the working principles of these devices. Furthermore, another important element is the generation of the time-averaged potential which really helps to reduce as much as possible one of the dimensions to the condensate. As I will explain in this chapter, this tool makes more efficient the phase imprinting-technique.

This chapter starts with a brief theoretical introduction on solitons, vortices and the working principles of phase-imprinting technique. After this, I will describe the elements required to make the phase-imprinting method work.

3.1 Theoretical background

3.1.1 Solitons

Solitons are stable, localized waves which propagate through a nonlinear medium without spreading. They can appear in several contexts, such as the dynamic of waves, transport along DNA and other macromolecules, fiber optic communications, etc. Depending on the details of the governing nonlinear wave equation, two types of solitions can appear: bright and dark soliton. I will focus on the second type.

Dark solitons are characterized by a local density minimum and a sharp phase gradient of the wave function at the position of the minimum. The shape of the soliton does not

change, due to the balance between the repulsive atom-atom interaction trying to reduce the minimum and the phase gradient trying to enhance it.

A weakly interacting Bose-Einstein condensate follows a non-linear wave equation which allows the creation of solitons. In the limit of zero temperature, this wave equation is known as the Gross-Pitaevski equation [17]

$$i\hbar\frac{\partial}{\partial t}\psi(\vec{r},t) = \left(-\frac{\hbar^2}{2m}\nabla^2 + V(\vec{r}) + g|\psi(\vec{r},t)|^2 \right)\psi(\vec{r},t), \tag{3.1}$$

where ψ is the condensate wave function, V is the trapping potential, m is the atomic mass, $\hbar$ the reduced Planck constant and g is the strength of the atom-atom interaction.

Dark solitons in a homogeneous 1-dimensional BEC can be solved analytically. The wavefunction ψ_s of a dark soliton is given by [18]

$$\psi_\mathrm{s}(x) = \sqrt{n_0}\left(i\frac{v_s}{c} + \sqrt{1-\frac{v_s^2}{c^2}}\tanh\left[\frac{x-x_s}{l_0}\sqrt{1-\frac{v_s^2}{c^2}}\right]\right), \tag{3.2}$$

where, $n_0 = |\psi_0|^2$ is the unperturbed density profile, v_s is the speed of the soliton, c is the Bogoliubov speed of the sound $c = \sqrt{n_0 g/m}$, x_s is the position of the nodal plane and $l_0 = \hbar/\sqrt{mn_0 g}$ is the correlation length. One of the main characteristic of a dark soliton is that its velocity is less than the Bogoliubov speed of sound . The soliton speed v_s can be expressed in terms of either the phase step δ or the soliton depth n_s, which is the difference between the unperturbed density n_0 and the density at the bottom of the "hole" [19]

$$\frac{v_s}{c} = \cos\left(\frac{\delta}{2}\right) = \sqrt{1-\frac{n_s}{n_0}}. \tag{3.3}$$

For $\delta = \pi$, the soliton has zero velocity, zero density in the center, and a discontinuous phase step. Since a dark soliton has a characteristic phase step, optically imprinting a phase step on the BEC wave function is a way to create a dark soliton. However, in 3-dimension, dark solitons exhibit thermodynamic and dynamical instabilities [18].

3.1.2 Vortices

Among phase defects studied in condensates, vortices are the most prominent. In this context, a vortex is a hole in the condensate, with the condensate circulating around the hole axis. If we redefine the time-independent wave function of the BEC as $\psi(\vec{r}) = f(\vec{r})\exp[i\phi(\vec{r})]$, then the velocity of the condensate $\vec{v}$ is given by

$$\vec{v} = \frac{\hbar}{m}\nabla\phi(\vec{r}), \tag{3.4}$$

and immediately $\nabla\times\vec{v} = 0$ that is, the velocity is irrotational, unless $\phi(\vec{r})$ has a singularity. Around a closed contour the change $\Delta\phi(\vec{r})$ in the phase of the wave function must be

multiple of 2π. Then the circulation Γ around a closed contour satisfies

$$\Gamma = \oint \vec{v} \cdot d\vec{l} = \frac{\hbar}{m} 2\pi l = l\frac{h}{m}, \tag{3.5}$$

where l is an integer, and so the circulation is quantized in units of h/m. Assuming a purely azimuthal flow in a rotational-invariant trap about the z-axis. To satisfy the requirement of single-valuedness, the wave function has to vary as $\exp[il\varphi]$, where φ is the azimuthal angle. Then, the velocity is [20]

$$v_\varphi = l\frac{\hbar}{m\rho}, \tag{3.6}$$

where ρ is the distance from the axis of the trap. The circulation is thus lh/m if the axis is enclosed by the contour, and zero otherwise. If $l \neq 0$, the wave function vanishes on the axis of the trap, since otherwise the kinetic motion would diverge. The result is that the structure of the flow pattern corresponds to a vortex [20].

3.1.3 Phase-imprinting method

In order to create topological states, we use the phase-imprinting technique. This technique modifies the phase distribution of the BEC by exposing it to pulsed, detuned laser with an intensity pattern $I(x, y)$. Then, the atoms experience a spatially varying light potential $U(x, y)$ described by (2.11) and acquire a corresponding phase. The wavefunction then transforms into [19]

$$\psi \to \psi \exp\left(\frac{-iU(x,y)t}{\hbar}\right), \tag{3.7}$$

where t is the time of the laser pulse. This time has to be short enough to make the atomic motion negligible during the imprinting.

In figure 3.1, I show the patterns required to create a vortex and a dark soliton, respectively. The first pattern imprints an azimuthally varying phase pattern with a 2π phase shift on the central top part. The second one generates a phase-shift. Taking this into account,equation (3.7) and (2.11) can be used to estimate the power and detuning required for the laser source.

3.2 Experimental set-up

In this section I will describe the elements required to build the phase-imprinting set-up.

3.2.1 Spatial light modulator

A SLM is a transmissive or reflective device which spatially modulates the amplitude and phase of an optical wavefront. Our SLM is provided by Digital Light Innovations and

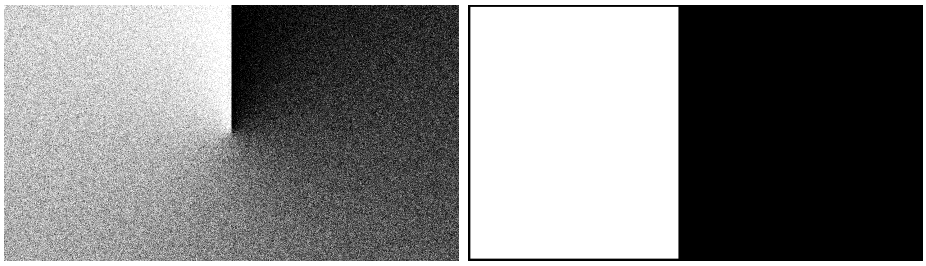

(a) (b)

Figure 3.1: Simple patterns which create a vortex (a) and a dark soliton (b)

contains a 0.95" 1080p Digital Micromirror Device (DMD) which is part of the Texas Instruments D4100 developer's kit [21].

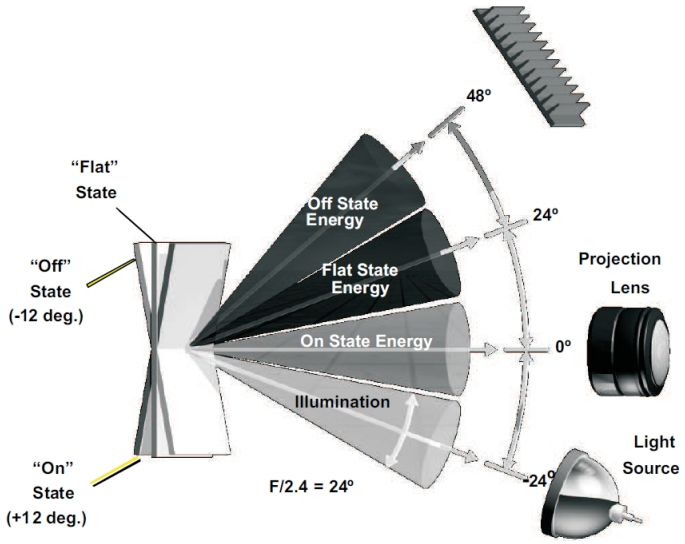

Figure 3.2: Angles of projection required for each mirror state [3].

The DMD is the optical component of the SLM. It possesses a 1920×1080 mirror screen with a pitch of 10.8 μm and a fill factor of 92.5%. Each mirror tilts with an angle of 12° and is based on complementary metal-oxide-semiconductor (CMOS) technology. So, the two possible states are ±12° to the optical axis. The best way of illuminating the SLM is to provide the incident light at an angle of -24° so that the *on state* (+12°) is perpendicular to the surface. The light resulting from the floating states presents an angle of +24°, and the *off state* (-12°) is then at +48°. This is shown in figure 3.2.

Moreover, the mirrors have a little gap between each other that allows them to rotate independently. However, this gap may have a negative effect on the contrast ratio of the device causing some diffraction when is illuminated with coherent light. The efficiency of the device is around 67%, so one has to act carefully if high-power illumination is required, which fortunately it is not our case.

To illustrate an example of the patterns that the device can create I show, in figure 3.3, an arbitrary pattern used to make initial tests. It was obtained with a light source of 780 nm wavelength at 100 μmW of power recorded with a CCD camera.

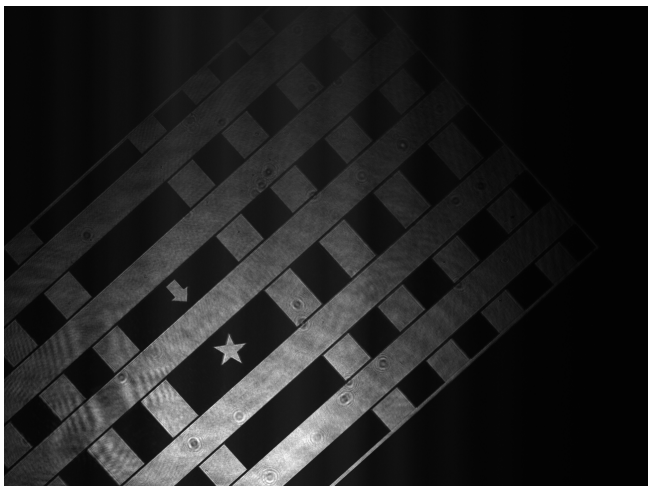

Figure 3.3: Picture of one patterns used to test the SLM. Specifically, it corresponds to the pattern demagnified by 1:4 factor.

3.2.2 Demagnifying optical system

Initially, we are interested in being able to impose the pattern when the atoms are trapped in the dipole potential at the end of the evaporation. It means without expansion time. In this situation, the sample is approximately 60 μm long. To imprint the light pattern onto the BEC, the light from the DMD has to be demagnified in order to have a similar size of the atom cloud. This is achieved by using a combination of **tube lens** and a **microscope objective**.

The **microscope objectives** available in our laboratory are the M-plan APO $\times 5$, $\times 10$, and the G-Plan $\times 20$ and $\times 50$ [22]. Their characteristics are shown in table 3.1. The numerical aperture is the range of angles over which the objective can accept or emit light. The parfocal length is the distance between the back of the objective and the location where it focuses. The working distance is the distance from the top of the objective to the position where it focuses. The depth of field is the range along the imaging path where the image is optimally focused. And, finally, the resolution is defined by the Rayleigh criteria $R = 1.22\lambda/2NA$, where λ is the wavelength of the light, and NA is the numerical aperture.

According to the technical documentation, the distance l required between the tube lens and the microscope objective can approximately be calculated by

$$l = \frac{f_2(\phi_2 - \phi_1)}{\phi}, \tag{3.8}$$

where $\phi_1 = 2f_1NA$ is the objective exit pulpil diameter, f_1 is the focal length of the microscope objective, $\phi_2 = 24$ mm and$f_2 = 200$ mm are the tube lens clear aperture and

Model	Numerical Aperture NA	Working Distance WD [mm]	Parfocal Length PL [mm]	Focal length f [mm]	Resolution R [μm]	Depth of focus DF [μm]
M Plan APO ×5	0.14	34.0	95	40	2.0	15.0
M Plan APO ×10	0.28	33.5	95	20	1.0	3.5
G Plan APO ×20	0.28	30.6	96.19	10	1.0	3.5
G Plan APO ×50	0.50	15.08	96.19	4	0.6	1.1

Table 3.1: Characteristics of the microscope objectives provided by the technical documentation. The resolving and focal depth of the discrete objective are values determined using $\lambda = 780$ nm.

focal length respectively, and ϕ is the size of the image field. The tube lens has $\phi_2 = 24$ mm and $f_2 = 200$ mm. The values obtained by equation (3.8) are shown in the table 3.2.

Model	ϕ_1 [mm]	l [mm]
M Plan APO ×5	11.2	284.4
M Plan APO ×10	11.2	284.4
G Plan APO ×20	5.6	408.8
G Plan APO ×50	4.0	444.4

Table 3.2: Results provided by equation (3.8) using $\phi = 9.0$ mm, which corresponds to the size of the camera used to test the objectives.

Model	l [mm]	WD [mm]
M Plan APO ×5	170	40
	225	38
	298	38
M Plan APO ×10	260	33
	340	35
	443	35
G Plan APO ×20	165	31
	257	31
	362	30
G Plan APO ×50	165	17

Table 3.3: Experimental working distances of each objective depending on distance l.

Furthermore, the working distance of each objective has been measured. To do that, we have used a target chart, specifically, the 1951 USAF resolution test chart whose design provides numerous small targets shapes exhibiting a stepped assortment of precise spatial frequency specimens [23]. The measurements of the working distance, depending on the distance l are shown in table 3.3. According to the manufacturer, a distance smaller than the ones given by (3.8) does not affect the optical performance [22]. This has been checked since all tests have been done in that way. However, if the distance is higher, it can produce shading. Finally, we will start using the ×50 in order to have a more precise

focus. But we could easily change in case it was needed. In figure 3.4, we can see two pictures of the test chart being seen through the ×50 microscope objective.

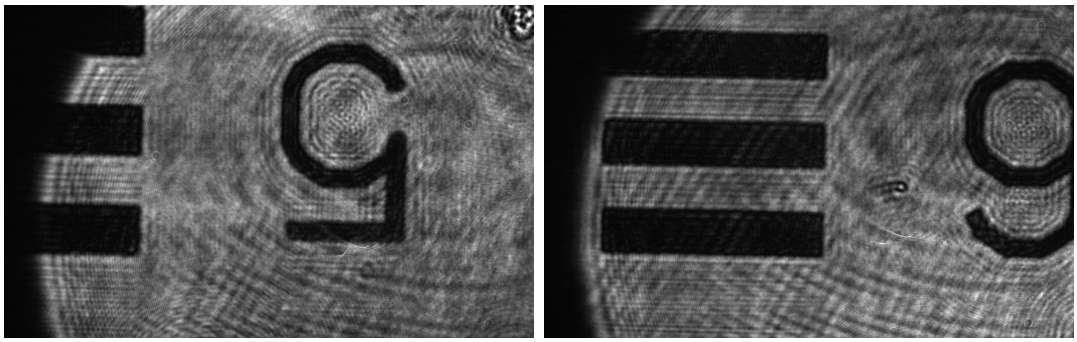

(a) (b)

Figure 3.4: The 1951 USAF resolution test chart being seen through the ×50 objective.

3.2.3 The final set-up

After the description of the elements needed for the phase-imprinting apparatus, I will describe here the final configuration, which is schematically shown in figure 3.5(a). I also show, in (b), a picture of the experiment where these elements are excatly placed. The light source consists of a DFD temperature-tunable laser diode centered at a wavelength of 780 nm, and it is sent to the SLM via fiber coupling. The reflected light (the light pattern) is first demagnified by a 1:4 telescope, and then is demagnified again using the ×50 microscope objective. All the optical elements involved must be perfectly aligned in order to focus the pattern on the plane of the atomic cloud. The width of the pattern is around 60 μm, which is similar to the size of the cloud without expansion time. In order to take the picture, another microscope objective is used (in the contrary direction) to magnify the light and record it in a CCD camera. In the figure, this objective is labeled as ×20. In practice, it gives enough resolution but it can be perfectly changed depending on the purposes. This set-up is similar to the one used in [24] for imprinting dark solitons.

3.2.4 2-dimensional potential

To make the phase-imprinting method more efficient, we additionally have to reduce one dimension of the system as much as possible. In other words, to create a quasi-2-dimensional BEC. As I have said in the section on theoretical background, phase-impriting consists in imposing a phase shift onto the whole condensate, and therefore, it would be easier if the system had one dimension less. So, being capable of generate a quasi-2-dimensional sample will make the realization of topological states more effective.

Quasi-2-dimensional BEC is achieved by vertically squeezing and making an expansion in the horizontal plane. To do that, I have implemented a different evaporation cooling step in the experimental sequence. First of all, vertically squeezing the atomic sample

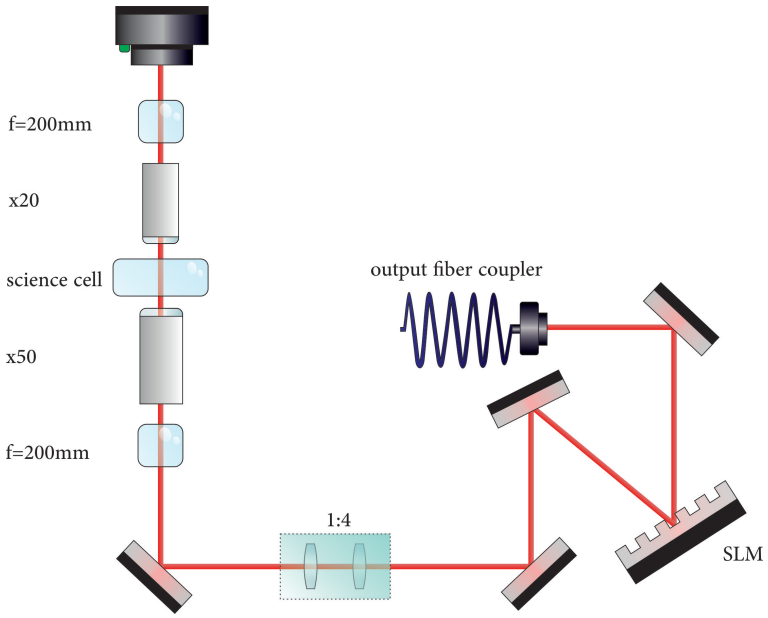

(a)

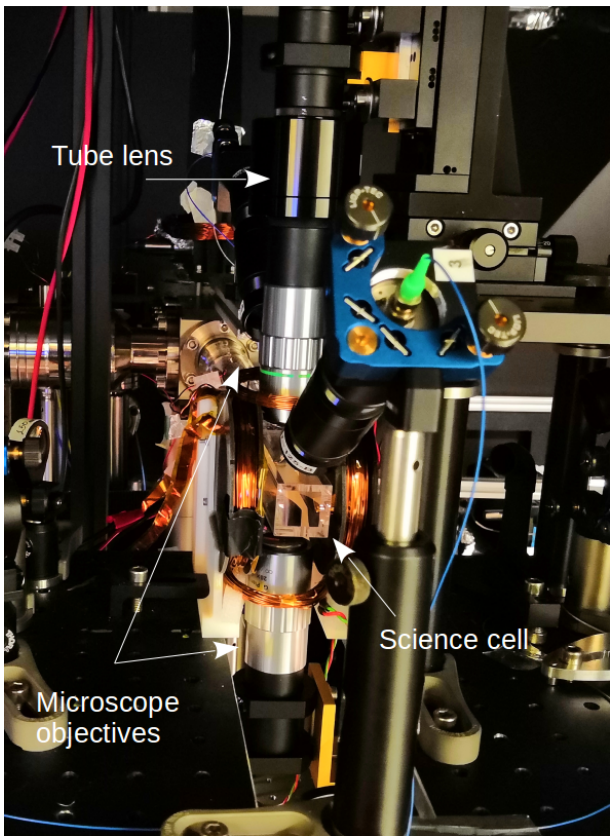

(b)

Figure 3.5: Schematic representation (not to scale) of the phase-impriting set-up (a). one dimension of the system as much as possible. Picture of the front part of the experiment, where the microscope objectives are placed (b).

means increasing the corresponding trapping frequency in this direction, which, at the end, means increasing the power. On the other hand, the expansion over the horizontal plane is produced by the action of a time-averaged dipole potential.

In the previous chapter, I have shown how the dipole potential can be approximated by a harmonic potential (2.17), and how to calculate the trapping frequencies (2.18) which characterise it. Starting from equations (2.18), after some calculations we get

$$\omega_z^2 = c_0 \frac{P_1}{w_{1,0}^4} + c_1 \frac{P_2}{w_{2,0}^4}, \tag{3.9}$$

$$\omega_y^2 = c_2 \frac{P_1}{w_{1,0}^4} + c_3 \frac{P_2}{w_{2,0}^4} + c_4 \frac{P_2}{w_{1,0}^4 w_{2,0}^2}, \tag{3.10}$$

$$\omega_x^2 = c_5 \frac{P_1}{w_{1,0}^6} + c_6 \frac{P_2}{w_{2,0}^4} + c_7 \frac{P_2}{w_{1,0}^4 w_{2,0}^2}, \tag{3.11}$$

where $\{c_i, i = 0, 1, \ldots, 7\}$ are constant values, P_i and $w_{i,0}$ are the power and waist respectively of the 1070 mm laser (1) and 1550 mm laser (2). As we can see, each frequency depends on both the power and the waist of each laser. Considering now that the sizes of the condensate scales as [16]

$$r_i \propto \frac{\omega_{ho}^{1/5}}{\omega_i} \sim \frac{1}{\omega_i}, \quad i = x, y, z, \tag{3.12}$$

where $\omega_{ho} = (\omega_x \omega_y \omega_z)^{1/3}$, an increment of ω_z and a decrease of ω_x and ω_y mean a squeezing in the vertical direction and an expansion in the horizontal plane. Therefore, it is needed to implement a new step in the sequence and, specifically, at the end of the evaporative cooling step. Then, simultaneously, the power of the 1070 nm laser is increased and its position starts to be oscillated. The fast spatial-oscillation creates a time-averaged potential which can be understood as the static potential generated by a fixed laser with a bigger waist [25] (this consideration has been used in theoretical calculations). So, in that way, $w_{1,0}$ and P_1 increase.

Generation of the time-averaged potential

The time-averaged potential is generated by using the acousto optical modulator (AOM). Depending on the frequency input in the AOM, the angle of the first diffracted order will change. So, if the AOM is feeded with a sinusoidal signal, then the angle of the first order will continuously change giving rise to an average-time potential when the oscillation is fast enough. Specifically, the AOM (Isomet M1080-T80L) works at 80 MHz frequency provided by the VCO (ZOS-150+). The sinusoidal signal, generated by an external function generator (Keysight 33500B Series), which is sent to the VCO input, has an amplitude of $2.25 V_{pp}$ and 24 kHz frequency. This frequency is similar to the one used in other experiments that can be found in the literature [19]. In figure 3.7(a), I show the intensity profile of the fast modulated 1070 nm beam on the CCD camera. The irregularities appear due to the fact that the efficiency of the AOM is not the same for

every frequency. This affects the amount of atoms that can be trapped. Therefore, we could improve the confinement with a compensation signal. For compensation, another sinusoidal signal is sent to the VVA (ZX73-2500- S+) with 48 KHz frequency, 240 mV_{pp} amplitude, and an offset of -140 mV. A bias-tee (ZX86-12G-S+) mixes the compensation signal with the initial VVA input to generate the new input. Essentially, the compensation signal increases the intensity of the laser when the efficiency of the AOM is lower. In figure 3.6, I schematically show the circuit to generate the time-averaged potential.

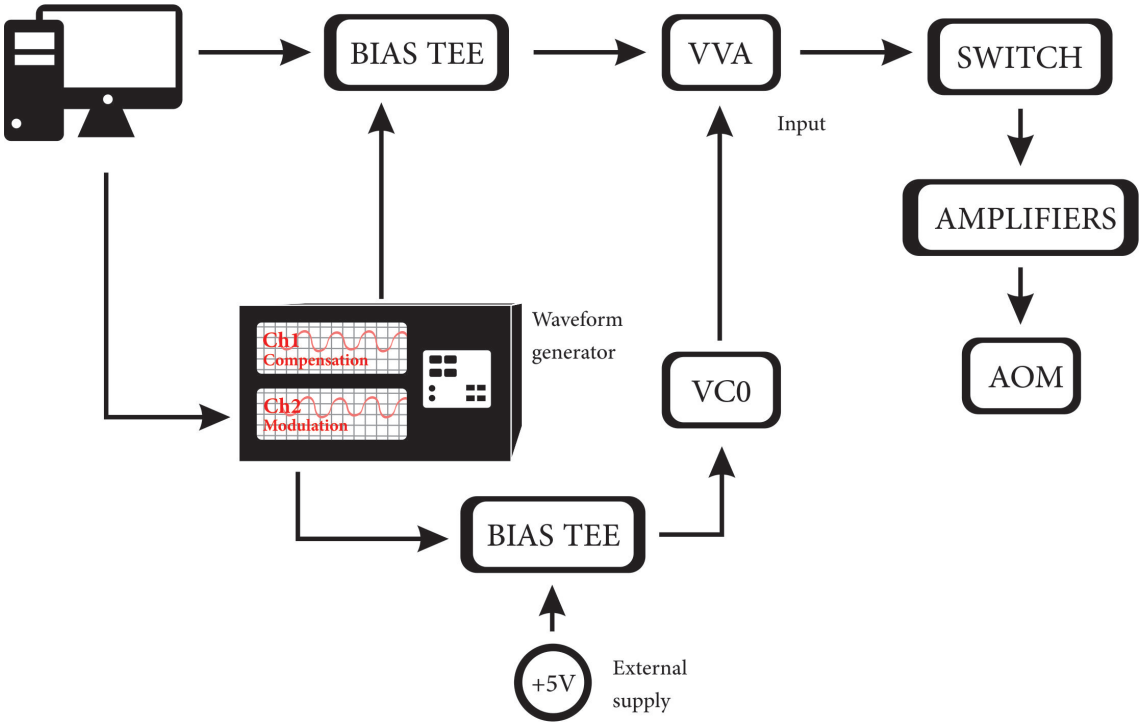

Figure 3.6: Circuit to generate quasi 2-dimensional potentials.

In figure 3.7, I show two time-averaged potential recorded by the CCD camera, and their projections onto the x-axis. Unlike case (a), in case (b) a compensation signal is applied, and so, the profile is almost perfectly flat. The fitting of the profile has been done using the following equation

$$f(x) = \frac{c_0}{2}\left(\frac{1}{1+\exp\left[-(x-c_1)/c_2\right]} + \frac{1}{1+\exp\left[(x-c_3)/c_4\right]} - 1\right), \tag{3.13}$$

where $\{c_i, i = 0, \ldots 4\}$ are the fitting parameters. This function has been proposed to reproduce both tails in the extremes of the profile as well as the plateau in the medium part. As we can see, this function nicely fits the density profile, and therefore, the potential can be perfectly characterised.

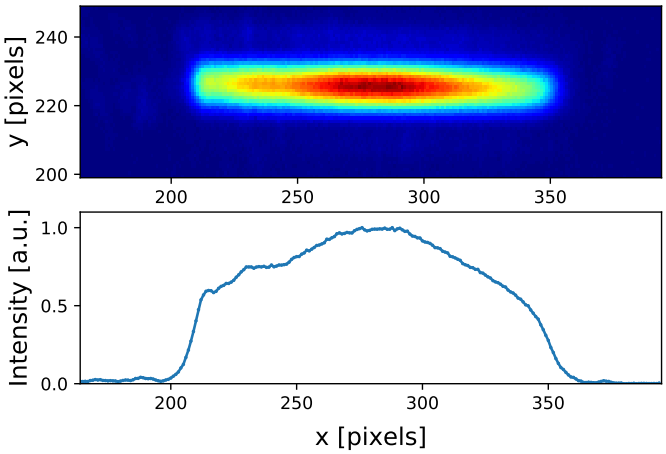

(a)

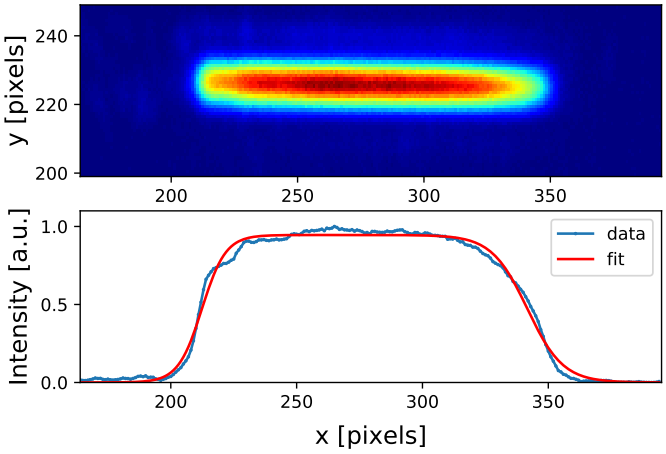

(b)

Figure 3.7: Time-averaged potential formed by rapidly scanning the 1070 nm gaussian beam with a frequency of 24 kHz without compensation (a) and with compensation (b). The figure of the top is the density profile of the potential recorded by the CCD camera. The bottom one corresponds to the projection over the x axis. The profile in (b) has been fitted using equation (3.13) showing a very good agreement.

Implementation in the experiment

I have explained how to create the time-averaged potential but now the key is how to implement it into the sequence. As I mentioned before, a new step has been included at the end of the evaporative cooling. There, the signal sent to the AOM consists of a sinusoidal modulation with monotonically increasing amplitude as a result of the combination of an external function generator (Keysight 33500B Series) and the Cicero Word Generator in the computer. The first one generates a constant sinusoidal signal, and the second one imposes the increasing amplitude modulation. At the same time, the power of the 1070 nm laser is increased until 600 mW, and the power of the 1550 nm laser is reduced until 10 mW. This step has a duration of 5 seconds. After, the oscillation is kept during another 100 ms and the power of both lasers remain constant. The duration of the step

and the values of the power have been chosen as a result of an optimisation procedure. This procedure consists of trying to get the maximum number of atoms and the maximum value of the phase space density. I present, in figure 3.8, the BEC sample trapped in the time-averaged potential without time of flight. The samples normally have now 30 - 50 $\times$ 10^3 atoms to be compared to 90 - 110 $\times$ 10^3 atoms before, but it is still a good number and enough for our purposes. The trapping frequencies of the sample are approximately $\omega_x = 2\pi\times$ 30 rad/s, $\omega_y = 2\pi\times$50 rad/s and $\omega_z = 2\pi\times$ 255 rad/s.

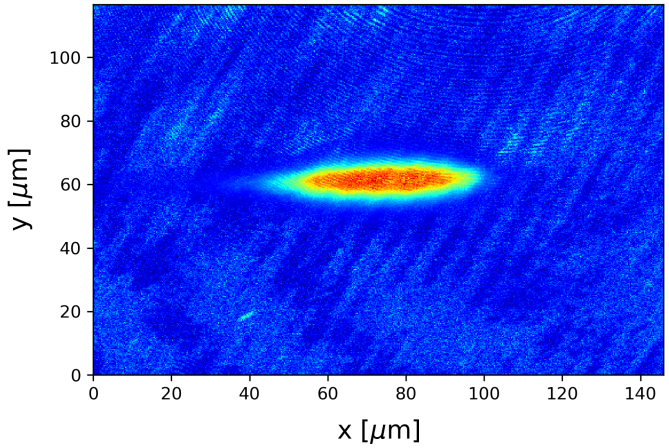

Figure 3.8: Quasi-2-dimensional Bose-Einstein Condensate of ^{87}Rb atoms without time of flight.

Chapter 4

Imprinting dark solitons

In this chapter, I will show some of the results that I could obtain. Dark solitons are generated by imprinting a local phase onto a quasi 2-dimensional BEC. By monitoring the density profiles I have studied the dynamics of this topological state. It has been observed how the density minimum, the peak of the soliton travels through the condensate with a constant velocity.

We apply an optical potential U generated by the dipole potential of a far-resonant laser source, to one half of the condensate wavefunction. We measure the distance after propagation between the position of the density minimum and the position of the imprinted phase step. Due to the random variation of the position of the sample from one shot to the next one, we could not always exactly apply the phase step at the center of the cloud. So, before taking any measurement, we first aligned very carefully the position of the imprinting pattern with a few shots, as an initial test.

4.1 Data analysis

Dimensional density profiles are obtained by absorption imaging technique, as I have explained in the first chapter. In order to make the analysis easier, 1-dimensional density profiles are calculated as a result of projecting the 2-dimensional density profile over the x-axis. These profiles have been fitted using the following equation

$$f(x) = \frac{p_0 - p_5}{2}\left(\frac{1}{1+\exp[-p_1(x-p_2)]} + \frac{1}{1+\exp[p_3(x-p_4)]} - 1\right) + p_5 - \frac{p_6}{\sqrt{2\pi p_6^2}}\exp\left(-\frac{(x-p_7)^2}{2p_6^2}\right), \tag{4.1}$$

where $p_i > 0$, $i = 0, 1, \ldots 7$ are the fitting parameters. This equation consists of two sigmoid functions to reproduce the limits of the profile, and a gaussian function to reproduce the soliton. p_7 is the center of the soliton, *i. e.*, the position of the local minimum.

To calculate an 8-parameter fitting for several data requires a non-negligible compu-

tational effort. So, to reduce this computational effort, I have designed an appropriate algorithm, in Python environment, to make this procedure as efficient as possible. First of all, the algorithm would need a seed composed of 8 different values, one for each parameter on the fit equation. Since I had to analyse several density profiles, the seed has to be as general as possible and valid for every case, otherwise I would have to manually set any of them. The idea is to be able to estimate some good candidates for the fit and use them as the seed. In that way, the computational effort will be much less, and the algorithm will get more easily the *a priori* non-predictable parameters. So, this can be solved by extracting information for each profile: the maximum value, the center, the deviation, etc. Given a 2-dimensional density profile, the algorithm can be summarised as follows:

- Firstly, the region of the atomic cloud is selected from the picture. Then, the projection over the x-axis is done. This 1-dimensional density profile is what is fitted.
- Then, a least squares fitting is made using the part of equation (4.1) associated to the sigmoid functions which consists of 5-parameter fit problem. This function reproduces a plateau when the sigmoid functions reach the maximum value. As a result, the shape of the profile is known.
- Finally, another fitting is made using the whole equation (4.1). Now, there are a set of 8 parameters to be optimised, and so, the seed has to have the same dimension. The values obtained from the previous step are used now as the first 5 values of the seed. The rest ones are approximated using the error function of the previous fitting. The position of the maximum negative value of this function in the plateau zone is a good candidate for the position of the peak of the soliton.

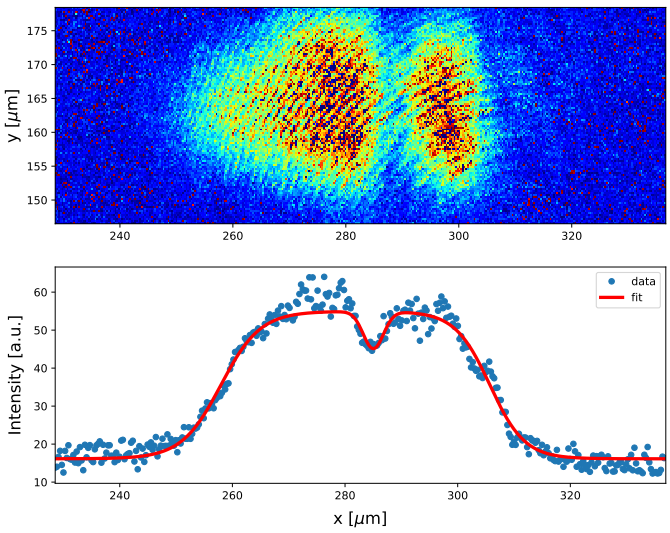

Figure 4.1: Density profile of the soliton in the quasi-2-dimensional BEC. The top picture is the 2-dimensional density profile (in arbitrary units) taken by absorption imaging. The bottom one is the 1-dimensional density profile obtained by the projection onto the x axis. The fitting has been done following equation (4.1). Specifically, this soliton has been measured 9 ms after imprinting a phase step.

In figure 4.1, I show the 2-dimensional density profile of the BEC with a soliton and its correspondent 1-dimensional density profile fitted with equation (4.1).

4.2 Results

Initially, we have tried to reproduce dark solitons with similar conditions from previous published results [18, 19, 24, 26]. We can find in the literature a wide variety of conditions in which solitons can be generated. For instance, regarding the wavelength of the light source, both far-resonant and close-resonant wavelengths are valid to make the imprinting technique work. So, our light source, which is centered in 780 nm is a good source. Moreover, the imprinting time is also different. This times vary from 1 μs [19] to 28 μs [18] although, in the first reference, solitons are generated in a sodium condensate. However, despite this diversity, these previous works give us an initial idea of the values of the parameters involved.

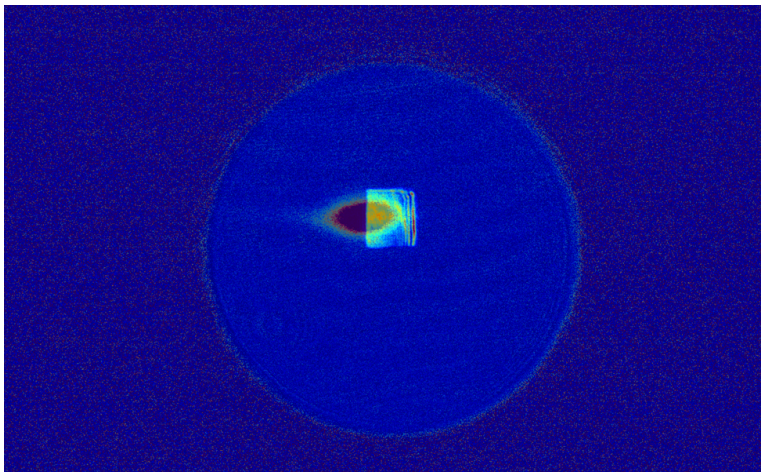

Figure 4.2: Overlap between the light pattern and the condensate. This picture consists of two indpendent pictures taken with the CCD camera subsequently superimposed.

To generate dark solitons, we impose the optical potential produced by a pattern light in one half of the wavefunction of the condensate when the atoms are trapped in the dipole potential. To efficiently make the phase-imprinting technique work, the pattern must be as more homogeneous as possible. However, despite our attempts, all optical aberrations could not be completely corrected. In figure 4.2, I show the overlapping between the pattern and the condensate without time of flight. As mentioned, it can be seen how the intensity is not constant over all the surface of the pattern due to optical aberrations. Since it could not be improved further than this, we decided to continue despite this issue.

First of all, we tried to generate dark solitons by imposing a phase step of $\sim \pi$ rad taking into account equations (3.7) and (2.11) to calculate the required conditions: power of the pattern light (or intensity), imprinting time and wavelength of the light source. The area of the pattern is constant, and consists of the half screen of the SLM which, in

the atom plane, has a dimensions of 37 x 32 μm^2. For simplicity, in this calculation, we have assumed that the intensity of the pattern is constant and completely homogeneous. With a phase step of π, the dark soliton is expected to have 0 velocity and so, to remain in the center of the cloud.

We started by fixing the time of the order of a few microseconds, from 1 to 50, and then, setting the pairs of values of power and wavelength from the calculations. However, we did not get any successful result following this procedure. They were unsatisfactory, showing complex structures far to be a soliton, with many instabilities and without any apparent pattern. After a careful check of all the set-up, we decided to experimentally scan the parameters involved in order to see some effect. An extensive work has been done in this direction. The wavelength is fixed by the temperature controller, the power of the light pattern is varied by a $\lambda/4$ waveplate (measured with the CCD camera), and the imprinting time is scanned shot to shot using Cicero. When the time scan is finished, the power is changed keeping the same wavelength, and another time scan is done. After finishing the power scan, then the wavelength is changed, and therefore, the procedure is repeated.

4.2.1 Dynamic of dark solitons

I show here some of the good results that I could get. To compare them with the experimental results, I also have performed some simulations. The parameters used in these simulations are shown in table 4.1. The algorithm of these simulation will be briefly explain in appendix A. In these simulations, I have calculated the dynamics of a dark soliton depending on the applied phase-shift, ranging from 0.1π to 1.9π rad. This phase-shift has been always applied to the right-half of the wavefunction. Results of this simulations shown that a phase step lower than π rad travels to the right; whereas a phase step bigger than π rad, to the left. This is plotted in figure 4.3.

Number of atoms N	$4 \cdot 10^4$
Trapping frequencies (ω_x, ω_y, ω_z)	$2\pi\times$(30, 40, 255)
Grid size (n_x, n_y, n_z)	(256, 16, 256)

Table 4.1: Parameters used in the simulation, which are the typical parameters in the experiment.

In figure 4.4, I show the time evolution of a dark soliton experimentally obtained. 2-dimensional density profiles for different times are shown (a). From top to bottom, t= 0.0, 1.0, 2.0, 3.0 ms. In (b), the result of the simulation having imposed a phase step of 1.74π for the same times respectively. To experimentally generate this soliton the parameters has been set as P =24 μW, λ = 780.3 nm and t = 200 μs. The resultant velocity of the soliton for both cases is 1.36 mm/s. Moreover, we could create dark solitons for different conditions. Their dynamic are shown in figures 4.5, 4.6 and 4.7. The first one corresponds to the case shown in 4.4. The contour plots show the evolution of the 1-dimensional density profiles denoting the position of the peak. The other figure shows the position of the peak respect to the position of the phase step. These points have been

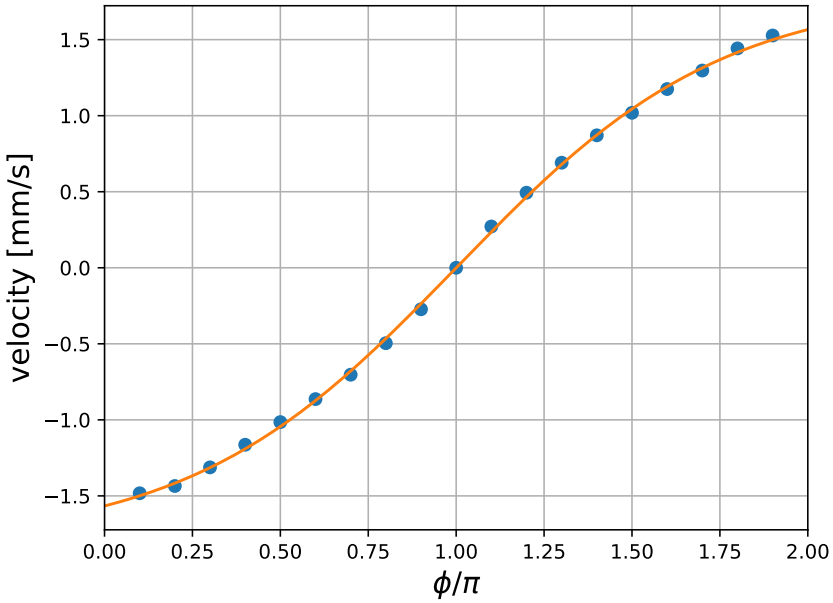

Figure 4.3: Velocities of the dark soliton depending on the phase step ϕ .The phase step has been imposed in the right half of the wavefunction. Negative values mean that the soliton travels to the right; and positive, to the left.

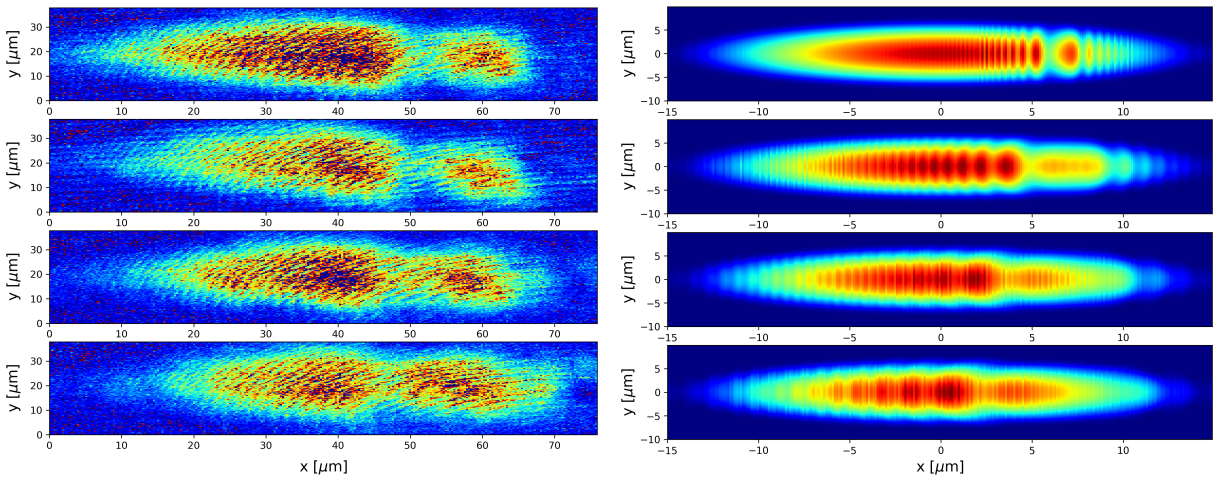

(a) (b)

Figure 4.4: Example of the time evolution of a dark soliton. (a) From up to down, experimental 2-dimensional density profiles for t= 0.0, 1.0, 2.0, 3.0 ms. The time of flight is set in 9 ms. (b) Theoretical 2-dimensional density profiles for the same times. The soliton is generated by imposing a phase step of 1.74π .

fitted with a linear regression in order to calculate the velocity of propagation. Error bars have been obtained following the error propagation rules. In the table below 4.2, I collect the conditions for each case and the velocity as a result of the analysis:

#	Wavelength [nm]	Power [μW]	Imprinting time [μs]	**Velocity [mm/s]**	Figure
1	780.5	24	200	**1.36 $\pm$ 0.05**	4.5
2	780.5	20	65	**1.24 $\pm$ 0.07**	4.6
3	780.5	35	200	**1.40 $\pm$ 0.16**	4.7

Table 4.2: Different conditions for the generation of dark solitons. It has been also included the velocity obtained from the linear regression.

Comparing the velocities obtained with the numerical simulations, we can associate the correspondent phase step which generates the correspondent velocities:

1. $v = 1.36$ mm/s $\rightarrow \phi = 1.74\pi$ rad.
2. $v = 1.24$ mm/s $\rightarrow \phi = 1.64\pi$ rad.
3. $v = 1.40$ mm/s $\rightarrow \phi = 1.78\pi$ rad.

However, using the equation of the dipole potential (2.11), the respective values of the phase-step ϕ would be 11.48π, 3.11π and 16.74π rad which, due to periodicity, are equivalent to 1.48π, 1.11π, 0.74π. This discrepancy is undoubtedly due to the assumption about the homogeneity of the pattern light. This fact makes impossible to calculate the real intensity applied to the condensate. Therefore, in this condition solitons cannot be completely experimentally characterised yet. However, the velocities obtained are in agreement with the possible velocities of the solitons that we can reproduce according to the simulations, and are also similar to the ones reported in previous publications.

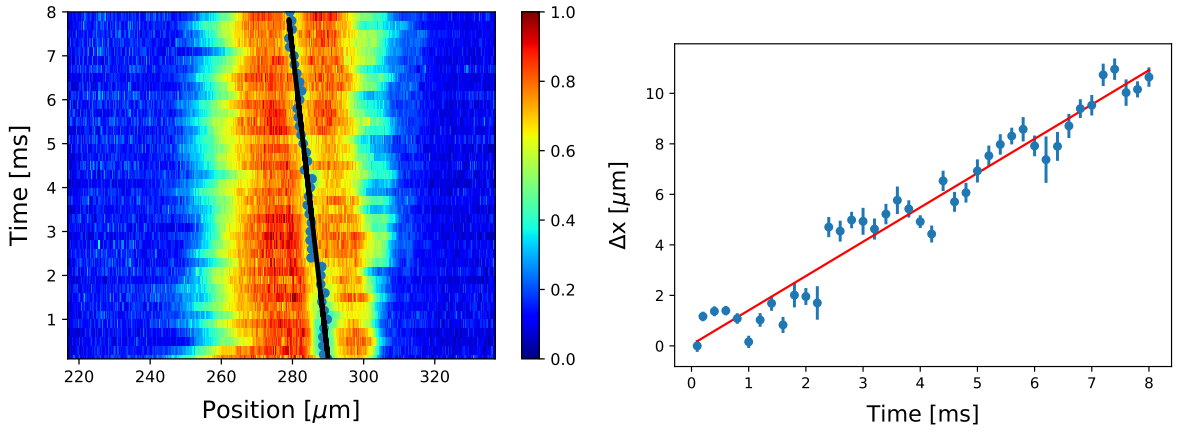

(a) (b)

Figure 4.5: Dynamic of a dark soliton. (a) 1-dimensional density profiles for various times after imprinting the phase step with a power of 24 μW in the right half of the condensate during 200 μs. Dots in the plot represent the position of center of the soliton. (b) Distance between the center of the soliton and the position of the imprinted phase step. The linear regression gives a velocity of 1.36 $\pm$ 0.05 mm/s. Time of flight has been set to 9 ms.

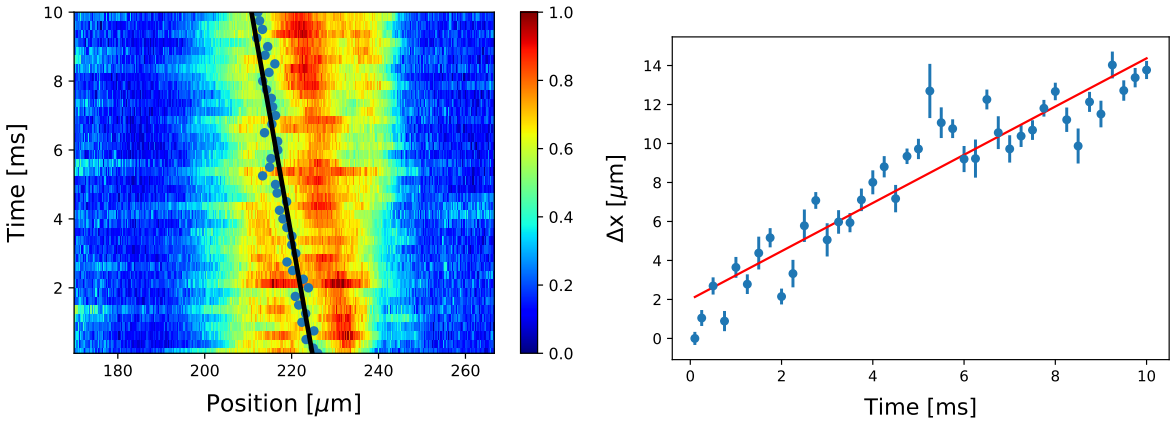

(a) (b)

Figure 4.6: Dynamics of a dark soliton. (a) 1-dimensional density profiles for various times after imprinting the phase step with a power of 20 μW in the right half of the condensate during 65 μs. Dots in the plot represent the position of center of the soliton. (b) Distance between the center of soliton and the position of the imprinted phase step. The linear regression gives a velocity of 1.24 $\pm$ 0.07 mm/s. Time of flight has been set in 9 ms.

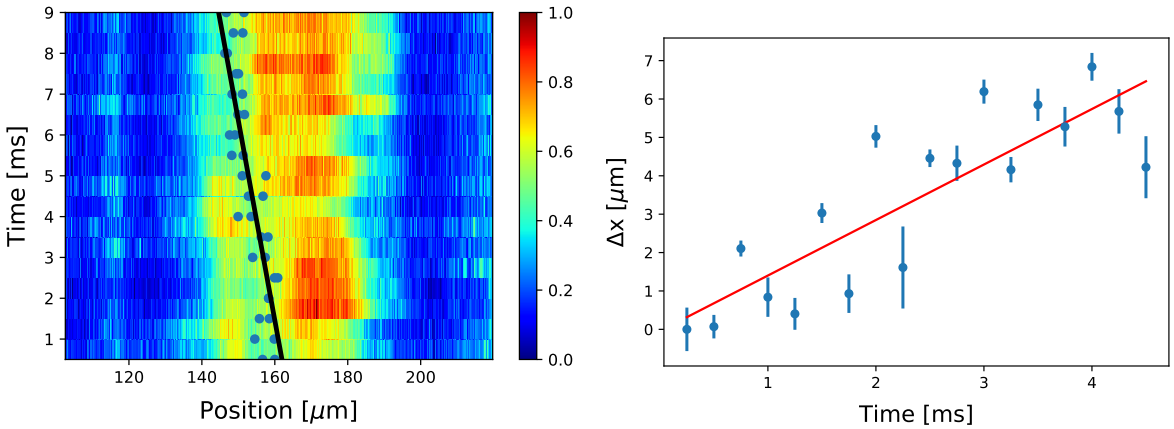

(a) (b)

Figure 4.7: Dynamic of a dark soliton. (a) 1-dimensional density profiles for various times after imprinting the phase step with a power of 35 μW in the right half of the condensate during 200 μs. Dots in the plot represent the position of center of the soliton. (b) Distance between the center of soliton and the position of the imprinted phase step. The linear regression gives a velocity of 1.40 $\pm$ 0.16 mm/s. Time of flight has been set in 9 ms.

Chapter 5

Conclusions

During the time I worked in the laboratory, I made several contributions. At the beginning, I focused on keeping the experiment in good condition by daily tests: power measurements, alignment of the optics, etc. These initial duties gave me the opportunity to get to know and understand the experimental set-up in detail. As I explained in the chapter 2, I modified some parts of the set-up. One of them was the full rotation of the 3D MOT which was necessary for the correct implementation of the phase-imprinting apparatus. Before that, there was not enough space to place the required optical elements. Other changes, such as the installation of a free-space optical path for the 1550 nm laser, improved the efficiency and the stability of the experiment, even with an increased number of atoms at the end of the evaporation. Furthermore, the modifications in the software *Cam Strip Down* allowed us to get the data more efficiently. However, my main contribution to the experiment has been the installation of the phase-imprinting apparatus. As explained in chapter 3, it consists of the spatial light modulator, the demagnifying optical system to focus the light pattern onto the atom plane, and the opto-electronic circuit to generate time-averaged potentials.

The phase-imprinting installation is the starting point to achieve the goals of the project: the study of complex non-linear dynamics over the condensate, of interest in several areas of Physics. Solitons are the simplest topological defect which can be generated in condensates. Since we can find in the literature several publications, both theoretical and experimental, about the creation and dynamics of solitons in condensates, we decided to generate solitons and to study their dynamics. Then, once we could produce preliminary results, we would continue to study other cases of greater complexity like vortices, pair or vortices, etc. So, the generations of solitons is a test to determine the functioning of the set-up. However, when the set-up was finally installed, I only spent one month in the laboratory before leaving the project. During this month, I worked extensively in order to make the set-up work and generate solitons. In the chapter 3, I have shown the best experimental results I could obtain.

Optical aberrations in the imprinting pattern were one of the most delicate issues. In the figure 4.2, I have shown the overlapping between the condensate and the light pattern. This picture also shows some optical aberrations in the pattern which produces

inhomogeneities of the intensity, and therefore, reduces the efficiency in the technique. Taking into account the fact that there are many very complex optical elements involved, such as the objective microscopes, any small deviations of the laser from the center of these elements could give rise to noticeable effects in the incoming light of the atoms. During the installation process, I was able to check the sensitivity of the alignment. However, although I worked hard to improve the alignment, a certain level of aberration still remained. For instance, the pattern used to create a soliton is made with the half of the screen of the DMD. Once we could get a soliton, I tried using the other half and there was no success. This shows that the beam was not perfectly aligned. However, since it is not necessary to use the whole screen, we did not worry about it at that time. I focused on correcting the aberrations using the good half of the screen. This still has to be corrected in the future for the generation of more complicated cases. Nevertheless, we could generate solitons and observe how they propagate over the condensate. Unfortunately, we could not exactly characterised the phase step imposed by the experimentally selected values. However, I could make the assignment between the velocity and the phase step according to the simulations performed.

By now, the set-up is still being optimised and, since I left, some changes have been done: the laser source to create the patterns has been replaced with a super luminescent diode with a wavelength of 830 nm. This light source, despite the fact that it is still incoherent, has a behaviour closer to a laser. Besides, the group members have decided to replaced the time-averaged potential with a flattened potential, since they started to have some problems with that. The flattened potential is created by using a cylindrical lens. However, there are no concrete results yet.

Appendix A

Simulations

To perform time-evolution simulations on the system, the time-dependent Gross-Pitaevskii equation is integrated. I have used two programs implemented in the Fortran language. The first one calculates the ground state of the system given the trapping frequencies and the number of atoms. The second one calculates the time evolution of the soliton over the condensate given the initial state: the system in the ground state with an imprinted phase-step. I briefly explain here the theoretical basis of the numerical approximations which can be found in [27].

A.1 Ground state

To determine the ground state of the GPE, imaginary time evolution is used. Imaginary time evolution can be performed by substituting $t \to \bar{t} = it$. As a result of this substitution, at each time step, all configurations are damped according to their energy, with configurations with larger energy being damped more heavily. After every imaginary time step, the number of atoms remain constant. By performing a sufficiently big number of imaginary time steps the ground state is well-approximated. However, a pure ground state is difficult to determine since energy levels are distributed continuously. To reduce the computational effort, the initial wave function is given by the Thomas-Fermi approximation. The Thomas-Fermi approximation is a very good approximation for the experimental spatial profile of the BEC.

A.2 Time evolution

The time-dependent GPE can be divided in two parts. One part depends on the position $\vec{x}$ in the grid, while the other one depends on the momentum $\hat{k} = i\nabla$. Thus, the equation is splitted according its spatial or momentum dependence

$$i\frac{\partial\psi}{\partial t} = \{L_1(\vec{x}) + L_2(\vec{k})\}\psi. \tag{A.1}$$

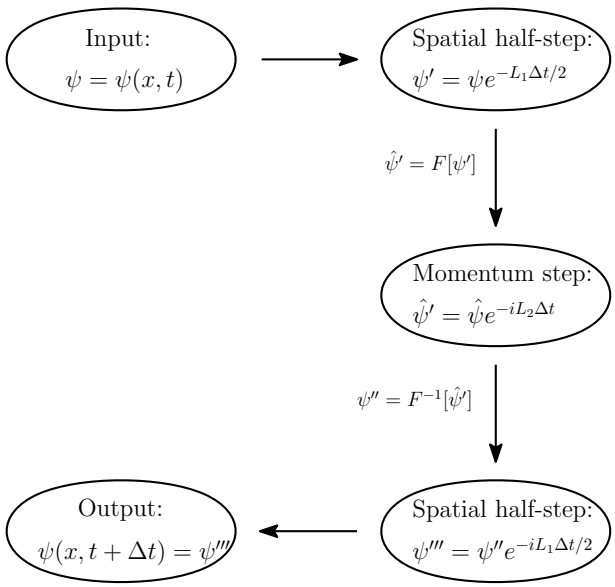

Figure A.1: Schematic representation of Strang Splitting Spectral Method.

Furthermore, the wavefunction ψ can be expressed in the k-basis by performing Fourier transform

$$\hat{\psi}(k) = F[\psi(x)](k). \tag{A.2}$$

Given a time step Δt, both the spatial and momentum dependent parts can be solved separately

$$i\frac{\partial}{\partial t}\psi(x,t) = L_1(x,t)\psi(x,t) \quad \rightarrow \quad \psi(x,t+\Delta t) = \psi(x,t)\exp\{-iL_1(x,t)\Delta t\}, \tag{A.3}$$

$$i\frac{\partial}{\partial t}\hat{\psi}(k,t) = L_2(k,t)\hat{\psi}(k,t) \quad \rightarrow \quad \hat{\psi}(k,t+\Delta t) = \hat{\psi}(k,t)\exp\{-iL_2(k,t)\Delta t\}. \tag{A.4}$$

Here, I have assumed that the time-step Δt is small enough to consider L_1 and L_2 constant over the length of the time step. To perform a full time step, it is necessary to consider both contributions. So, the Strang Splitting Spectral Method (SSSM) [28] is employed to take both contributions into account. Figure A.1 schematically shows the application of this method.

Bibliography

[1] D. Benedicto-Orenes. *Realization of a spin-1 Bose-Einstein condensate*. PhD thesis, University of Birmingham, 2018.

[2] D. J. McCarron. A guide to acousto-optic modulators. *http://massey. dur. ac. uk/resources/slcornish/AOMGuide. pdf*, 2007.

[3] Texas Instruments. DLP System Optics Diagram. `http://www.ti.com/general/docs/datasheetdiagram.tsp?genericPartNumber=DLP5500&diagramId=321`. Accessed: 2018-08-06.

[4] K. B. Davis, M. O. Mewes, M. R. Andrews, N. J. van Druten, D.S. Durfee, D. M. Kurn, and W. Ketterle. Bose-Einstein condensation in a gas of sodium atoms. *Physical review letters*, 75(22):3969, 1995.

[5] M. R. Matthew, B. P. Anderson, P. C. Haljan, D. S. Hall, C. E. Wieman, and E. A. Cornell. Vortices in a Bose-Einstein condensate. *Physical Review Letters*, 83(13):2498, 1999.

[6] S. Burger, K. Bongs, S. Dettmer, W. Ertmer, K. Sengstock, A. Sanpera, GV Shlyapnikov, and M. Lewenstein. Dark solitons in Bose-Einstein condensates. *Physical Review Letters*, 83:5198, 1999.

[7] V. L. Berezinskii. Destruction of long-range order in one-dimensional and two-dimensional systems possessing a continuous symmetry group. ii. quantum systems. *Soviet Journal of Experimental and Theoretical Physics*, 34:610, 1972.

[8] J. M. Kosterlitz and D. J. Thouless. Ordering, metastability and phase transitions in two-dimensional systems. *Journal of Physics C: Solid State Physics*, 6(7):1181, 1973.

[9] Z. Hadzibabic, P. Krüger, M. Cheneau, B. Battelier, and J. Dalibard. Berezinskii–Kosterlitz–Thouless crossover in a trapped atomic gas. *Nature*, 441(7097):1118, 2006.

[10] J. Nespolo, G.E. Astrakharchik, and A. Recati. Andreev–Bashkin effect in superfluid cold gases mixtures. *New Journal of Physics*, 19(12):125005, 2017.

[11] D. A. Steck. Rubidium 87 D line data, 2001.

[12] C. J. Foot. *Atomic physics*, volume 7. Oxford University Press, 2005.

[13] O. J. Luiten, M. W.Reynolds, and J. T. M. Walraven. Kinetic theory of the evaporative cooling of a trapped gas. *Physical Review A*, 53(1):381, 1996.

[14] R. Grimm, M. Weidemüller, and Y. B. Ovchinnikov. Optical dipole traps for neutral atoms. In *Advances in atomic, molecular, and optical physics*, volume 42, pages 95–170. Elsevier, 2000.

[15] M. D. Barrett, J. A. Sauer, and M. S. Chapman. All-Optical formation of an atomic Bose-Einstein condensate. *Physical Review Letters*, 87:010404, Jun 2001.

[16] W. Ketterle, D. S. Durfee, and D. M. Stamper-Kurn. Making, probing and understanding Bose-Einstein condensates. *arXiv preprint cond-mat/9904034*, 1999.

[17] F. Dalfovo, S. Giorgini, L. P. Pitaevskii, and S. Stringari. Theory of Bose-Einstein condensation in trapped gases. *Reviews of Modern Physics*, 71(3):463, 1999.

[18] S. Burger, K. Bongs, S. Dettmer, W. Ertmer, K. Sengstock, A. Sanpera, G. V. Shlyapnikov, and M. Lewenstein. Dark solitons in Bose-Einstein condensates. *Physical Review Letters*, 83(25):5198, 1999.

[19] J. Denschlag, J. E. Simsarian, D. L. Feder, C. W. Clark, L. A. Collins, J. Cubizolles, L. Deng, E. W. Hagley, K. Helmerson, W. P. Reinhardt, S. L. Rolston, B. I. Schneider, and W. D. Phillips. Generating solitons by phase engineering of a Bose-Einstein condensate. *Science*, 287(5450):97–101, 2000.

[20] C. J. Pethick and H. Smith. *Bose–Einstein condensation in dilute gases*. Cambridge university press, 2008.

[21] Texas Instruments. Discovery D4100 developer's kit. `http://www.ti.com/tool/DLPD4X00KIT#descriptionArea`. Accessed: 2018-08-06.

[22] Mitutoyo Japan. Universal Measuring microscope MF-U. `https://www.mitutoyo.co.jp/eng/support/service/catalog/04/E14003.pdf`. Accessed: 2018-08-06.

[23] Thorlabs. R3L3S1P - Positive 1951 USAF Test Target, 3" x 3". `https://www.thorlabs.com/drawings/dc88b6dba526ba4a-A2B94829-BB70-D3AB-1B7509DC1540BB0F/R3L3S1N-AutoCADPDF.pdf`. Accessed: 2018-08-06.

[24] N. Meyer, H. Proud, M. Perea-Ortiz, C. O'Neale, M. Baumert, M. Holynski, J. Kronjäger, G. Barontini, and K. Bongs. Observation of two-dimensional localized Jones-Roberts solitons in Bose-Einstein condensates. *Physical Review Letters*, 119(15):150403, 2017.

[25] T. A. Bell, J. A. P. Glidden, A. P. Jake, L. Humbert, M. W J. Bromley, S. A. Haine, M. J. Davi, T. W. Neely, M. A. Baker, and H. Rubinsztein-Dunlop. Bose–Einstein condensation in large time-averaged optical ring potentials. *New Journal of Physics*, 18(3):035003, 2016.

[26] C. Becker, S. Stellmer, P. Soltan-Panahi, S. Dörscher, M. Baumert, E. M. Richter, J. Kronjäger, K. Bongs, and K. Sengstock. Oscillations and interactions of dark and dark–bright solitons in Bose–Einstein condensates. *Nature Physics*, 4(6):496, 2008.

[27] J. Smits. *Phase imprinting of vortices in Bose-Einstein condensates using shaped light*. PhD thesis, Utrecht University, 2016.

[28] M. Thalhammer. Time-splitting spectral methods for nonlinear Schrödinger equations, Spring School 2009.